

# Towards an Improved Experimental Joint Identification in Frequency-Based Substructuring

Jure Korbar <sup>a</sup>, Domen Ocepek<sup>a</sup>, Miha Pogačar <sup>a</sup>, Gregor Čepon <sup>a,\*</sup>

<sup>a</sup>University of Ljubljana, Faculty of Mechanical Engineering, Aškerčeva cesta 6, 1000 Ljubljana, Slovenia

## Publication:

Korbar, J., Ocepek, D., Pogačar, M., and Čepon, G. (2025). Towards an improved experimental joint identification in frequency-based substructuring. *Mechanical Systems and Signal Processing* (<https://doi.org/10.1016/j.ymssp.2025.113115>).

---

## Abstract

The dynamic behavior of assembled structures is strongly influenced by the dynamic properties of connections between the individual substructures, commonly referred to as joints. Accurately predicting assembly dynamics relies on identifying joint properties, which are influenced by factors such as preload, temperature, and vibration amplitude. These interactions make analytical and numerical modeling challenging, necessitating an experimental modeling approach. This study presents a joint identification framework inspired by the Lagrange multiplier frequency-based substructuring, along with four mutually independent modifications to the identification approach. These modifications comprise sparse regression, rigid-body mode constraints, excitation direction updating, and indirect parametrization. A parametrization-based approach is employed for estimating the mass, damping, and stiffness properties of the joint. The numerical and experimental results highlight the benefits of each modification and demonstrate the effectiveness of the proposed framework for robust joint property estimation.

**Keywords:** joint identification, regularization, virtual point transformation, impact excitation, dynamic substructuring

---


## 1. Introduction

Assembly dynamics can be estimated by combining dynamic models of the individual components through the compatibility of connecting interface displacements and the equilibrium of interface forces, also known as dynamic substructuring (DS) [1]. However, connections within real structures are often complex, as they rely on connecting elements that may not strictly satisfy these idealized constraints. This makes DS predictions inaccurate, especially in cases where resilient elements are used to connect individual substructures. This type of connection further deviates from the traditional exact compatibility constraints typically assumed in DS, and thus requires more sophisticated modeling approaches. Two main strategies have been widely adopted to account for real-world connections, namely the transmission simulator (TS) [2] and joint identification, although they are generally not interchangeable as each of the two typically serves a distinct purpose. The TS approach introduces an additional TS substructure into the substructuring procedure in order to replicate the interface conditions which are present in the final assembly. By adjusting the DS procedure to include the additional substructure, the interface conditions are implicitly accounted for, improving the prediction of assembly dynamics.

Alternatively, the dynamic properties of the interface connections can be identified separately in what is known as joint identification, where the connections between individual substructures are referred to as

---

\*Corresponding author

Email address: [gregor.cepon@fs.uni-lj.si](mailto:gregor.cepon@fs.uni-lj.si) (Gregor Čepon )

joints [3]. Instead of assuming idealized rigid joints, the identified dynamic properties of the joints are used to indirectly couple the individual substructures. Joint identification strategies generally rely on measuring the assembly dynamics and isolating the joint by removing the effects of the individual substructures [3]. Since the final assembly is often not available during virtual prototyping, a separate test assembly can be utilized, where the connections between the individual substructures should accurately replicate the connections between the substructures in the final assembly [4]. This approach is especially suitable for virtual prototyping, e.g. to design resilient mounts with the desired dynamic properties, or when modifying several substructures within an assembly [5]. Care should be taken to ensure the interface conditions are accurately replicated, including potential preloads, vibration amplitude, temperature, etc. [6]

Typical joint identification methods thus require obtaining the frequency-response functions (FRFs) of the assembly and its individual components. Tsai and Chou developed a method for joint identification based on measured FRFs, where the joint was described in terms of stiffness and damping parameters while neglecting the joint mass [3]. Their approach assumed incompatible interface displacements, forming a gap at the interface between the individual substructures. The joint produces reaction forces opposing the opening of the interface gap. Wang and Liou used a similar set of assumptions in [7] and addressed the problem of measurement errors by introducing an improved joint identification approach with the aim of reducing the number of inverse matrix operations. In the presence of measurement noise, their method improved the identification consistency, as matrix inversion can lead to magnification of noise and measurement errors, typical for ill-conditioned matrices. Ren and Beards presented a parametrization-based approach which modeled the joint as a separate substructure within an assembly [8]. In addition to the inclusion of an interface gap, they also eliminated the interface force equilibrium constraint. If the joint mass is significant, the interface forces of the adjacent substructures are no longer in equilibrium. Therefore, their approach allowed for the inertial properties of the joint to be accounted for. The authors continued their work by addressing the problem of stiff joints by combining the above approach with substructure coupling to identify only the compliant joints [9]. Yang et al. modeled the joint only in terms of a stiffness matrix [10]. Both translational and rotational degrees of freedom (DoFs) were accounted for in their formulation, including cross coupling terms, which refer to the relationship between non-collocated DoFs. Čelič and Boltežar extended the joint identification method of Ren and Beards by considering rotational DoFs and demonstrated that neglecting rotational DoFs can lead to a decrease in identification accuracy [11]. The authors also analyzed the influence of the reduction of internal and joint DoFs on joint identification consistency [12]. They demonstrated that it is not feasible to reduce the joint DoFs if a parametrized joint model is considered. Wang et al. modeled the joint in terms of its admittance matrix and derived an approach for joint identification similar to the method proposed by Ren and Beards [13]. Their method was augmented by estimating the unmeasured assembly FRFs to further overdetermine the identification. Batista et al. presented an iterative approach to joint identification and developed a frequency selection criterion relying on the matrix condition number [14]. Mehrpouya et al. investigated two methods for joint identification, namely the inverse receptance coupling (IRC) and the point-mass model [15]. Both methods considered the joint in terms of linear springs and dampers without cross coupling terms and included the joint mass. The IRC method proved to be advantageous due to significantly lower computation time and reduced experimental effort. The IRC method was later extended for the identification of multiple joints in [16] by considering only the out-of-plane stiffness and damping parameters of the joints. Mehrpouya et al. also applied joint identification to 3D structures in [17], where the cross-coupling terms were accounted for.

Meggitt et al. used an inverse substructuring (IS) approach to obtain the joint and the individuals substructures' dynamics by measuring only the assembly dynamics [18], which was demonstrated on resiliently coupled structures. A twelve DoF model of rubber isolators was obtained in [6] using frequency-based substructuring (FBS), as well as IS. Although FBS can be more generally applied, measurements of the individual substructures and the assembly are required, while IS requires only measurements of the assembled structure. The approach utilized the virtual point transformation (VPT) [19] to include rotational DoFs of the joint. The VPT assumes the interface motion can be described by a set of interface deformation modes (IDMs). This allows to apply a geometric transformation to the measured interface DoFs to obtain a set of virtual point (VP) DoFs described by the selected IDMs.

The introduction of system equivalent model mixing (SEMM) allowed to expand a set of measured FRFs

at easily accessible locations to inaccessible interface DoFs of a numerical model to improve its accuracy in a hybrid model [20]. SEMM has been modified to allow for joint identification by iteratively expanding the measured assembly dynamics to the estimated assembly dynamics obtained by coupling the individual substructures with the joint model from the previous iteration. By subsequently decoupling the substructures from the hybrid model, an improved joint model is obtained. This procedure is repeated until convergence [21, 22, 23, 24]. Additional efforts have been made to reduce errors and improve identification accuracy [25, 26].

A prerequisite for consistent joint identification is a suitable representation of the interface, i.e. selecting the appropriate number of interface DoFs, which was demonstrated in [27]. Apart from the number of interface DoFs, it is important to select the appropriate type of interface description, especially when dealing with continuous interfaces [28]. In addition, the appropriate choice of compatibility and equilibrium conditions can significantly improve decoupling accuracy [29].

The identification of bolted joints receives significant attention, as they are commonly used to connect individual parts [4, 30, 31]. Due to their significant influence on assembly dynamics, joint identification remains an active topic of research, with the recent works focusing on the robustness of the identification [32], viscoelasticity [33], welded joint properties [34], and rubber isolators [35]. Advancements in machine learning have also facilitated the adoption of data-driven approaches in structural dynamics, including joint identification [36] and structural health monitoring [37].

A common challenge linked to joint identification is the measurement inaccuracies and noise polluting the measurements, adversely affecting the identified joint. Similarly, inconsistencies between the dynamic properties of the substructures in the assembly and the individual substructure models in the uncoupled state result in decoupling error, which propagates to the identified joint model [38, 39]. This study focuses on obtaining a physical-domain representation of the joint, also known as joint parametrization. To allow for the coupling of arbitrary substructures, a twelve-DoF joint model is adopted [6]. A reformulation of the Ren and Beards' approach in [8] is presented, inspired by the Lagrange multiplier frequency-based substructuring (LM-FBS). To address the issues associated with measurement inaccuracies, four procedures are proposed with the aim of improving the accuracy of the identified joint:

1. Sparsity of the joint model is promoted by applying the Least Absolute Shrinkage and Selection Operator (LASSO) [40]. The significance of some parameters in the traditional least-squares (LS) procedure may be caused by measurement errors. The aim of applying LASSO is to neglect these terms and therefore improve the identification consistency.
2. Modeling the interface using the VPT requires knowing locations and directions of measured response and excitation DoFs [19]. Since sensor locations can be replicated with reasonable accuracy, the errors are assumed to be predominantly caused by inaccurate impact excitation [41]. With well-spaced excitations, the relative location error decreases, while excitation directions errors remain unchanged. In this case, excitation inaccuracy is dominated by excitation direction errors. An iterative algorithm for excitation direction updating is proposed, which is applied prior to the joint identification.
3. The direct application of LS (or LASSO) to obtain the joint parameters may result in a physically inconsistent joint model. For the proposed twelve-DoF joint model, no force should be required to perform rigid-body motion if the joint mass is neglected. Therefore, the damping and stiffness matrices should be constrained such that rigid-body motion requires no force, resulting in rank deficiency of these matrices.
4. The formulation in [8] directly performs joint parametrization based on the measured FRFs. An alternative approach is proposed by splitting the formulation in [8] to first directly identify the dynamic stiffness matrix of the joint, followed by the parametrization.

All of the above procedures are mutually independent, allowing for arbitrary combinations, resulting in 16 distinct approaches. All 16 approaches are first assessed in the numerical study, followed by an experimental study, in order to validate the results of the numerical study. The remainder of the paper is organized as follows: Section 2 summarizes the theory of joint identification based on measured FRFs and joint parametrization. Section 3 describes the four modifications aiming at improving the joint identification

accuracy. Section 4 presents the numerical study with the results and corresponding discussion. The experimental study is described in Section 5, including experimental results and discussion. Finally, conclusions are drawn in Section 6.

## 2. Joint identification in the physical domain

The beginning of this section briefly introduces the notation used in this paper. Following the notation used in [1], the frequency-domain equation of motion, relating the displacements of a structure to the external forces, is written as:

$$\left(-\omega^2 \mathbf{M}^{(s)} + j\omega \mathbf{C}^{(s)} + j\mathbf{D}^{(s)} + \mathbf{K}^{(s)}\right) \mathbf{u}^{(s)}(\omega) = \mathbf{f}^{(s)}(\omega), \quad (1)$$

where  $\mathbf{u}^{(s)}(\omega)$  and  $\mathbf{f}^{(s)}(\omega)$  respectively denote the frequency-dependent vectors of displacement and external force.  $\mathbf{M}^{(s)}$ ,  $\mathbf{C}^{(s)}$ ,  $\mathbf{D}^{(s)}$ , and  $\mathbf{K}^{(s)}$  are the mass, viscous damping, structural damping, and stiffness matrices,  $\omega$  denotes the excitation angular frequency, and the superscript  $\star^{(s)}$  denotes a quantity pertaining to the substructure  $(s)$ . Defining the sum of the matrices in Eq. (1) as the frequency-dependent dynamic stiffness matrix  $\mathbf{Z}^{(s)}(\omega)$  allows the equation of motion to be written as:

$$\mathbf{Z}^{(s)}(\omega) \mathbf{u}^{(s)}(\omega) = \mathbf{f}^{(s)}(\omega). \quad (2)$$

By inverting the impedance matrix  $\mathbf{Z}^{(s)}(\omega)$ , the equation of motion can be expressed in terms of the admittance matrix  $\mathbf{Y}^{(s)}(\omega)$ :

$$\mathbf{u}^{(s)}(\omega) = \mathbf{Y}^{(s)}(\omega) \mathbf{f}^{(s)}(\omega), \quad \text{where} \quad \mathbf{Y}^{(s)}(\omega) \triangleq \left(\mathbf{Z}^{(s)}(\omega)\right)^{-1}. \quad (3)$$

Expressing the equation of motion by considering Eq. (3) is experimentally advantageous, as each term in  $\mathbf{Y}^{(s)}(\omega)$  contains a single FRF, which can be easily obtained by measuring the responses to known excitation forces. With the aim of improving readability, the remainder of the paper will omit explicitly denoting the frequency dependence.

### 2.1. Joint isolation

The joint identification formulation in this paper is inspired by the LM-FBS, however, it is mathematically equivalent to the approach presented in [8]. The derivation starts by obtaining the coupling equation and subsequently expressing the terms pertaining to the dynamic stiffness of the joint. First, the displacements, forces, and admittance matrices are defined:

$$\mathbf{u} = \begin{bmatrix} \mathbf{u}^A \\ \mathbf{u}^B \end{bmatrix}, \quad \mathbf{f} = \begin{bmatrix} \mathbf{f}^A \\ \mathbf{f}^B \end{bmatrix}, \quad \mathbf{g} = \begin{bmatrix} \mathbf{g}^A \\ \mathbf{g}^B \end{bmatrix}, \quad \mathbf{Y}^{A|B} = \begin{bmatrix} \mathbf{Y}^A & \\ & \mathbf{Y}^B \end{bmatrix}, \quad (4)$$

where  $\mathbf{g}$  and  $\mathbf{Y}^{A|B}$  denote the vector of connecting interface forces and the uncoupled block-diagonal admittance matrix, containing admittance matrices of substructures A and B. Furthermore, the DoFs are partitioned into interface and internal DoFs:

$$\mathbf{u}^A = \begin{bmatrix} \mathbf{u}_1^A \\ \mathbf{u}_2^A \end{bmatrix}, \quad \mathbf{u}^B = \begin{bmatrix} \mathbf{u}_3^B \\ \mathbf{u}_4^B \end{bmatrix}, \quad \mathbf{f}^A = \begin{bmatrix} \mathbf{f}_1^A \\ \mathbf{f}_2^A \end{bmatrix}, \quad \mathbf{f}^B = \begin{bmatrix} \mathbf{f}_3^B \\ \mathbf{f}_4^B \end{bmatrix}, \quad \mathbf{g}^A = \begin{bmatrix} \mathbf{0} \\ \mathbf{g}_2^A \end{bmatrix}, \quad \mathbf{g}^B = \begin{bmatrix} \mathbf{g}_3^B \\ \mathbf{0} \end{bmatrix}, \quad (5)$$

where subscripts  $\star_1$  and  $\star_4$  denote the internal DoFs, while subscripts  $\star_2$  and  $\star_3$  denote the interface DoFs of substructures A and B, respectively. The initial equation of motion is written as:

$$\mathbf{u} = \mathbf{Y}^{A|B} (\mathbf{f} + \mathbf{g}), \quad (6)$$

where the unknown forces  $\mathbf{g}_2^A$  and  $\mathbf{g}_3^B$  act on the interface DoFs of A and B, respectively. Taking into account the connecting interface forces  $\mathbf{g}$  in the uncoupled equation of motion applies the connecting forces  $\mathbf{g}$  to the interface, which effectively couples the substructures.

The joint is considered here as a separate substructure, with its equation of motion written in the impedance form:

$$\mathbf{Z}^J \mathbf{u}^J = \boldsymbol{\lambda} \quad \Leftrightarrow \quad \begin{bmatrix} \mathbf{Z}_{22}^J & \mathbf{Z}_{23}^J \\ \mathbf{Z}_{32}^J & \mathbf{Z}_{33}^J \end{bmatrix} \begin{bmatrix} \mathbf{u}_2^J \\ \mathbf{u}_3^J \end{bmatrix} = \begin{bmatrix} \boldsymbol{\lambda}_2 \\ \boldsymbol{\lambda}_3 \end{bmatrix}, \quad (7)$$

where  $\boldsymbol{\lambda}$  denotes the interface forces of the substructures A and B acting on the joint. The impedance formulation allows to neglect arbitrary terms in the joint's system matrices without sacrificing the existence of its admittance matrix due to rank-deficiency of the impedance matrix.<sup>1</sup> The term system matrices refers to the set of mass, stiffness, viscous damping, and structural damping matrices of the joint for the remainder of the paper.

In order to obtain the coupled admittance matrix, the unknown interface forces  $\mathbf{g}$  must be eliminated from Eq. (6). The joint identification problem assumes the substructures A and B are not directly attached to one another, but are connected by a joint. Coupling A and B with the joint requires satisfying the interface displacement compatibility and interface force equilibrium constraints:

$$\begin{bmatrix} \mathbf{u}_2^A \\ \mathbf{u}_3^B \end{bmatrix} = \begin{bmatrix} \mathbf{u}_2^J \\ \mathbf{u}_3^J \end{bmatrix}, \quad (8a)$$

$$\begin{bmatrix} \mathbf{g}_2^A \\ \mathbf{g}_3^B \end{bmatrix} + \begin{bmatrix} \boldsymbol{\lambda}_2 \\ \boldsymbol{\lambda}_3 \end{bmatrix} = \begin{bmatrix} \mathbf{0} \\ \mathbf{0} \end{bmatrix}. \quad (8b)$$

Inspired by the the LM-FBS formulation [1], two boolean matrices are defined to enforce the compatibility and equilibrium equations:

$$\mathbf{B}_u^J \mathbf{u} = \mathbf{u}^J, \quad (9a)$$

$$\mathbf{g} = -\mathbf{B}_f^{J\top} \boldsymbol{\lambda}. \quad (9b)$$

The joint forces are calculated by replacing  $\mathbf{u}^J$  in Eq. (7) with Eq. (9a) and are inserted into Eq. (9b):

$$\boldsymbol{\lambda} = \mathbf{Z}^J \mathbf{B}_u^J \mathbf{u}, \quad (10)$$

$$\mathbf{g} = -\mathbf{B}_f^{J\top} \mathbf{Z}^J \mathbf{B}_u^J \mathbf{u}. \quad (11)$$

The interface forces  $\mathbf{g}$  in Eq. (6) can now be eliminated:

$$\mathbf{u} = \mathbf{Y}^{A|B} \left( \mathbf{f} - \mathbf{B}_f^{J\top} \mathbf{Z}^J \mathbf{B}_u^J \mathbf{u} \right). \quad (12)$$

Next, the displacements  $\mathbf{u}$  are factored out:

$$\begin{aligned} \mathbf{u} &= \mathbf{Y}^{A|B} \mathbf{f} - \mathbf{Y}^{A|B} \mathbf{B}_f^{J\top} \mathbf{Z}^J \mathbf{B}_u^J \mathbf{u}, \\ \left( \mathbf{I} + \mathbf{Y}^{A|B} \mathbf{B}_f^{J\top} \mathbf{Z}^J \mathbf{B}_u^J \right) \mathbf{u} &= \mathbf{Y}^{A|B} \mathbf{f}, \\ \mathbf{u} &= \left( \mathbf{I} + \mathbf{Y}^{A|B} \mathbf{B}_f^{J\top} \mathbf{Z}^J \mathbf{B}_u^J \right)^{-1} \mathbf{Y}^{A|B} \mathbf{f}. \end{aligned} \quad (13)$$

The product of matrices multiplying the external forces in Eq. (13) represents the coupled admittance matrix  $\mathbf{Y}^{A|B}$ :

$$\mathbf{Y}^{A|B} = \left( \mathbf{I} + \mathbf{Y}^{A|B} \mathbf{B}_f^{J\top} \mathbf{Z}^J \mathbf{B}_u^J \right)^{-1} \mathbf{Y}^{A|B}. \quad (14)$$

Eq. (14) allows to couple the joint impedance with the admittance matrices of the individual substructures. If both the coupled and uncoupled admittance matrices are known, the joint can be identified by rearranging Eq. (14):

$$\mathbf{Y}^{A|B} \mathbf{B}_f^{J\top} \mathbf{Z}^J \mathbf{B}_u^J \mathbf{Y}^{A|B} = \mathbf{Y}^{A|B} - \mathbf{Y}^{A|B}. \quad (15)$$

---

<sup>1</sup>Describing the dynamics of a joint with free boundary conditions only in terms of a stiffness matrix prevents the calculation of the admittance matrix. Since the stiffness matrix requires no force to perform rigid-body displacements, the matrix is rank-deficient and therefore not invertible.

In [8], four equations for joint identification are presented, which are combined into a single equation here. The equivalence of Eq. (15) and the equations in [8] can be seen by pre-multiplying Eq. (15) by  $\mathbf{Y}^{\text{AJB}}\mathbf{Y}^{\text{A|B}}^{-1}$  and post-multiplying by  $\mathbf{Y}^{\text{AJB}}^{-1}\mathbf{Y}^{\text{A|B}}$ , providing the alternative form of Eq. (15):

$$\mathbf{Y}^{\text{AJB}}\mathbf{B}_f^{\text{J}\top}\mathbf{Z}^{\text{J}}\mathbf{B}_u^{\text{J}}\mathbf{Y}^{\text{A|B}} = \mathbf{Y}^{\text{A|B}} - \mathbf{Y}^{\text{AJB}}. \quad (16)$$

For the sake of consistency, the alternative form expressed in Eq. (16) is considered for the remainder of the paper.

## 2.2. Joint parametrization

The dynamic stiffness of the joint can be directly obtained by calculating the left and right inverse of  $\mathbf{Y}^{\text{AJB}}\mathbf{B}_f^{\text{J}\top}$  and  $\mathbf{B}_u^{\text{J}}\mathbf{Y}^{\text{A|B}}$ , respectively, however, we are interested in obtaining the system matrices of the joint, i.e. parametrizing the joint. Due to the high dynamic range of the FRFs in Eq. (16), the terms in the vicinity of the eigenfrequencies dominate the entire system of equations. Even if the equations are weighted per frequency, the response amplitudes can significantly deviate between the measured DoFs, therefore, additional weighing is advised to use the measured information more effectively. In [8], different weighting techniques were proposed. Consistent with their findings, it was observed that the Weighting-Before (transformation)-Group (equations) method (WBG) is advantageous. The WBG method calculates a frequency-dependent diagonal weighting matrix  $\mathbf{W}$ , where each term is calculated as the reciprocal of the root-mean-square value of the corresponding row in the product  $\mathbf{Y}^{\text{AJB}}\mathbf{B}_f^{\text{J}\top}$ . Eq. (16) is subsequently pre-multiplied by the matrix  $\mathbf{W}$ :

$$\mathbf{W}\mathbf{Y}^{\text{AJB}}\mathbf{B}_f^{\text{J}\top}\mathbf{Z}^{\text{J}}\mathbf{B}_u^{\text{J}}\mathbf{Y}^{\text{A|B}} = \mathbf{W}\mathbf{Y}^{\text{A|B}} - \mathbf{W}\mathbf{Y}^{\text{AJB}}. \quad (17)$$

Since all of the unknown variables are gathered in the matrix  $\mathbf{Z}^{\text{J}}$ , (column-major) vectorization is performed:

$$\left( \left( \mathbf{B}_u^{\text{J}}\mathbf{Y}^{\text{A|B}} \right)^{\top} \otimes \left( \mathbf{W}\mathbf{Y}^{\text{AJB}}\mathbf{B}_f^{\text{J}\top} \right) \right) \text{vec}(\mathbf{Z}^{\text{J}}) = \text{vec}(\mathbf{W}\mathbf{Y}^{\text{A|B}} - \mathbf{W}\mathbf{Y}^{\text{AJB}}), \quad (18)$$

where  $\otimes$  denotes the Kronecker product of the adjacent matrices and  $\text{vec}(\star)$  refers to the column-major vectorization of the matrix  $\star$ . For brevity, we define the following:

$$\begin{aligned} \mathbf{A}_1 &\triangleq \left( \mathbf{B}_u^{\text{J}}\mathbf{Y}^{\text{A|B}} \right)^{\top} \otimes \left( \mathbf{W}\mathbf{Y}^{\text{AJB}}\mathbf{B}_f^{\text{J}\top} \right), \\ \mathbf{y} &\triangleq \text{vec}(\mathbf{W}\mathbf{Y}^{\text{A|B}} - \mathbf{W}\mathbf{Y}^{\text{AJB}}). \end{aligned} \quad (19)$$

Writing the joint impedance matrix in terms of the system matrices leads to the joint parametrization:

$$\mathbf{Z}^{\text{J}} = -\omega^2\mathbf{M}^{\text{J}} + j\omega\mathbf{C}^{\text{J}} + j\mathbf{D}^{\text{J}} + \mathbf{K}^{\text{J}}. \quad (20)$$

Replacing the joint impedance in Eq. (18) with the system matrices is facilitated by rewriting Eq. (20) in the following form:

$$\mathbf{Z}^{\text{J}} = \mathbf{P}\mathbf{\Omega}, \quad \text{where} \quad \mathbf{P} \triangleq [\mathbf{M}^{\text{J}} \quad \mathbf{C}^{\text{J}} \quad \mathbf{D}^{\text{J}} \quad \mathbf{K}^{\text{J}}] \quad \text{and} \quad \mathbf{\Omega} \triangleq \begin{bmatrix} -\omega^2\mathbf{I} \\ j\omega\mathbf{I} \\ j\mathbf{I} \\ \mathbf{I} \end{bmatrix}. \quad (21)$$

Eq. (21) factors the dynamic stiffness into a frequency-dependent matrix  $\mathbf{\Omega}$  and a frequency-independent matrix  $\mathbf{P}$  containing the system matrices. This approach allows to express Eq. (18) at different frequencies using a single set of unknown variables. Eq. (21) is pre-multiplied by the identity prior to insertion into Eq. (20) to facilitate vectorization:

$$\begin{aligned} \mathbf{A}_1 \text{vec}(\mathbf{I}\mathbf{P}\mathbf{\Omega}) &= \mathbf{y}, \\ \mathbf{A}_1 (\mathbf{\Omega}^{\top} \otimes \mathbf{I}) \text{vec}(\mathbf{P}) &= \mathbf{y}. \end{aligned} \quad (22)$$

Again, for brevity, the above equation is rewritten as:

$$\mathbf{A}_1 \mathbf{A}_2 \text{vec}(\mathbf{P}) = \mathbf{y}, \quad \text{where} \quad \mathbf{A}_2 \triangleq \boldsymbol{\Omega}^\top \otimes \mathbf{I} \quad \text{and} \quad \text{vec}(\mathbf{P}) = \begin{bmatrix} \text{vec}(\mathbf{M}^J) \\ \text{vec}(\mathbf{C}^J) \\ \text{vec}(\mathbf{D}^J) \\ \text{vec}(\mathbf{K}^J) \end{bmatrix}. \quad (23)$$

Although Eq. (23) can be solved via LS, the solution may violate reciprocity of the system matrices. The system matrices should therefore be symmetric, which can be enforced by expressing the vectorized matrices as a product of a duplication matrix  $\mathbf{L}$  and the unique variables [42], also known as half-vectorization:

$$\text{vec}(\star) = \mathbf{L} \text{vech}(\star), \quad (24)$$

where  $\text{vech}(\star)$  denotes the half-vectorization of the square matrix  $\star$ , i.e. the vectorization of the lower-triangular part of the matrix  $\star$ . Eq. (23) can therefore be written as:

$$\mathbf{A}_1 \mathbf{A}_2 \mathbf{L}_p \mathbf{p} = \mathbf{y} \quad \Leftrightarrow \quad \mathbf{A} \mathbf{p} = \mathbf{y}, \quad (25)$$

where

$$\mathbf{L}_p \triangleq \begin{bmatrix} \mathbf{L} & & & \\ & \mathbf{L} & & \\ & & \mathbf{L} & \\ & & & \mathbf{L} \end{bmatrix}, \quad \mathbf{p} \triangleq \begin{bmatrix} m^J \\ c^J \\ d^J \\ k^J \end{bmatrix} \triangleq \begin{bmatrix} \text{vech}(\mathbf{M}^J) \\ \text{vech}(\mathbf{C}^J) \\ \text{vech}(\mathbf{D}^J) \\ \text{vech}(\mathbf{K}^J) \end{bmatrix}, \quad \text{and} \quad \mathbf{A} \triangleq \mathbf{A}_1 \mathbf{A}_2 \mathbf{L}_p. \quad (26)$$

Both  $\mathbf{A}$  and  $\mathbf{y}$  are frequency dependent, while  $\mathbf{p}$  is frequency independent. Therefore, Eq. (25) is stacked at different frequencies:

$$\begin{bmatrix} \mathbf{A}(\omega_1) \\ \vdots \\ \mathbf{A}(\omega_N) \end{bmatrix} \mathbf{p} = \begin{bmatrix} \mathbf{y}(\omega_1) \\ \vdots \\ \mathbf{y}(\omega_N) \end{bmatrix} \Leftrightarrow \mathbf{A}_\Omega \mathbf{p} = \mathbf{y}_\Omega, \quad (27)$$

where  $\star_\Omega$  represents the column-stacked vectors or matrices  $\star$  at frequencies in the set  $\Omega = \{\omega_1 \dots \omega_N\}$ . Both  $\mathbf{A}_\Omega$  and  $\mathbf{y}_\Omega$  are complex, while  $\mathbf{p}$  is real, therefore, the real solution for  $\mathbf{p}$  is found by splitting Eq. (27) into real and imaginary components:

$$\begin{bmatrix} \text{Re}(\mathbf{A}_\Omega) \\ \text{Im}(\mathbf{A}_\Omega) \end{bmatrix} \mathbf{p} = \begin{bmatrix} \text{Re}(\mathbf{y}_\Omega) \\ \text{Im}(\mathbf{y}_\Omega) \end{bmatrix}. \quad (28)$$

Solving Eq. (28) in a least-squares sense allows to identify the parameters of the joint with the reciprocity of the system matrices taken into account. This approach performs joint parametrization directly based on Eq. (16) and will be regarded as direct parametrization (DP) for the remainder of the paper. After solving Eq. (28), the vectorized system matrices can be calculated:

$$\text{vec}(\mathbf{P}) = \mathbf{L}_p \mathbf{p}. \quad (29)$$

### 3. Modifying the established joint identification approach

#### 3.1. Indirect joint parametrization

Alternatively, Eq. (16) can be used to calculate the frequency-dependent joint impedance  $\mathbf{Z}^J$ , effectively performing decoupling in the frequency domain:

$$\mathbf{Z}^J = \left( \mathbf{Y}^{\text{AJB}} \mathbf{B}_f^{\text{J}\top} \right)^+ \left( \mathbf{Y}^{\text{A|B}} - \mathbf{Y}^{\text{AJB}} \right) \left( \mathbf{B}_u^{\text{J}} \mathbf{Y}^{\text{A|B}} \right)^+. \quad (30)$$

The joint impedance matrix  $\mathbf{Z}^J$  can be calculated directly using Eq. (30). Following Eq. (21), the joint impedance can be parametrized, i.e. written in terms of the system matrices, and vectorized, taking into

account the symmetry of the system matrices. Again, to account for varying amplitude ranges, a frequency-dependent weighting matrix  $\mathbf{W}$  is introduced, such that each row in  $\mathbf{WZ}^J$  has unit variance:

$$\text{vec}(\mathbf{WZ}^J) = (\boldsymbol{\Omega}^\top \otimes \mathbf{W}) \mathbf{L}_p \mathbf{p}. \quad (31)$$

Denoting  $\text{vec}(\mathbf{WZ}^J)$  as  $\mathbf{y}$  and  $(\boldsymbol{\Omega}^\top \otimes \mathbf{W}) \mathbf{L}_p$  as  $\mathbf{A}$  allows to write the joint identification equation exactly as in (25):

$$\mathbf{A}\mathbf{p} = \mathbf{y}, \quad \text{where} \quad \mathbf{A} \triangleq (\boldsymbol{\Omega}^\top \otimes \mathbf{W}) \mathbf{L}_p \quad \text{and} \quad \mathbf{y} \triangleq \text{vec}(\mathbf{WZ}^J). \quad (32)$$

Again, joint parameters are solved for by stacking Eq. (32) at different frequencies and splitting the system into real and imaginary components. This alternative joint parametrization approach relies on first decoupling and subsequently parametrizing the joint, therefore, the approach will be regarded as indirect parametrization (IP).

### 3.2. Enforcing rank-deficiency

Apart from the reciprocity of the system matrices, there are additional requirements, which the identified joint may violate. Since the joint model should effectively couple the adjacent substructures, the joint itself should have free boundary conditions. Therefore, the stiffness and the damping matrices should not oppose any rigid-body motion of the joint, since only the inertial forces can oppose rigid-body motion. Applying an arbitrary rigid-body displacement  $\mathbf{u}_{\text{RB}}^J$  should therefore require no force [43]:

$$\mathbf{C}^J \dot{\mathbf{u}}_{\text{RB}}^J = \mathbf{0}, \quad (33a)$$

$$\mathbf{D}^J \mathbf{u}_{\text{RB}}^J = \mathbf{0}, \quad (33b)$$

$$\mathbf{K}^J \mathbf{u}_{\text{RB}}^J = \mathbf{0}. \quad (33c)$$

Any rigid-body displacement can be expressed as a superposition of the joint's rigid-body modes. Defining the rigid-body modes requires first defining the joint DoFs. A two-node joint model with six DoFs per node is adopted, schematically shown in Fig. 1, where the two joint nodes are separated by  $L$  units of distance.

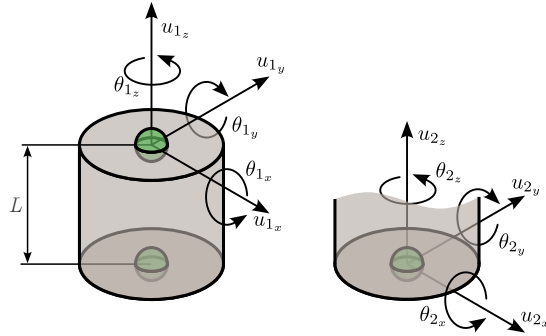


Figure 1: Definition of joint DoFs.

The set of joint DoFs  $\mathbf{u}^J$  is expressed as:

$$\mathbf{u}^J = \begin{bmatrix} \mathbf{u}_1^J \\ \mathbf{u}_2^J \end{bmatrix}, \quad \text{where} \quad \mathbf{u}_i^J = [u_{ix} \quad u_{iy} \quad u_{iz} \quad \theta_{ix} \quad \theta_{iy} \quad \theta_{iz}]^\top, \quad i \in \{1, 2\}. \quad (34)$$

Assuming small displacements and considering the definition of joint DoFs in Eq. (34) and in Fig. 1, any rigid-body displacement of the joint can be written as a superposition of the rigid-body modes<sup>2</sup>:

$$\mathbf{u}_{\text{RB}}^J = \mathbf{U}_{\text{RB}} \mathbf{q}_{\text{RB}}, \quad (35)$$

<sup>2</sup>The rigid-body modes in  $\mathbf{U}_{\text{RB}}$  are expressed such that they are easy to comprehend, although the selection of rigid-body modes is not unique. Nevertheless, care should be taken to ensure the selected modes can describe all viable rigid-body motion.

where

$$\mathbf{U}_{\text{RB}}^\top = \begin{bmatrix} 1 & 0 & 0 & 0 & 0 & 0 & 1 & 0 & 0 & 0 & 0 & 0 \\ 0 & 1 & 0 & 0 & 0 & 0 & 0 & 1 & 0 & 0 & 0 & 0 \\ 0 & 0 & 1 & 0 & 0 & 0 & 0 & 0 & 1 & 0 & 0 & 0 \\ 0 & -\frac{L}{2} & 0 & 1 & 0 & 0 & 0 & \frac{L}{2} & 0 & 1 & 0 & 0 \\ \frac{L}{2} & 0 & 0 & 0 & 1 & 0 & -\frac{L}{2} & 0 & 0 & 0 & 1 & 0 \\ 0 & 0 & 0 & 0 & 0 & 1 & 0 & 0 & 0 & 0 & 0 & 1 \end{bmatrix} \quad \text{and} \quad \mathbf{q}_{\text{RB}} = \begin{bmatrix} q_x \\ q_y \\ q_z \\ q_{\theta x} \\ q_{\theta y} \\ q_{\theta z} \end{bmatrix}. \quad (36)$$

Each row of  $\mathbf{U}_{\text{RB}}^\top$  represents a rigid-body mode, while the coordinates in  $\mathbf{q}_{\text{RB}}$  scale the rigid-body modes to obtain the displacements. Applying Eq. (35) to Eqs. (33) reads:

$$\mathbf{C}^J \mathbf{U}_{\text{RB}} \dot{\mathbf{q}}_{\text{RB}} = \mathbf{0} \quad \forall \quad \dot{\mathbf{q}}_{\text{RB}}, \quad (37a)$$

$$\mathbf{D}^J \mathbf{U}_{\text{RB}} \mathbf{q}_{\text{RB}} = \mathbf{0} \quad \forall \quad \mathbf{q}_{\text{RB}}, \quad (37b)$$

$$\mathbf{K}^J \mathbf{U}_{\text{RB}} \mathbf{q}_{\text{RB}} = \mathbf{0} \quad \forall \quad \mathbf{q}_{\text{RB}}. \quad (37c)$$

Since Eqs. (37) are valid for any  $\mathbf{q}_{\text{RB}}$ , the column space of rigid-body modes  $\mathbf{U}_{\text{RB}}$  must lie in the null space of matrices  $\mathbf{C}^J$ ,  $\mathbf{D}^J$ , and  $\mathbf{K}^J$ :

$$\mathbf{C}^J \mathbf{U}_{\text{RB}} = \mathbf{0}, \quad \mathbf{D}^J \mathbf{U}_{\text{RB}} = \mathbf{0}, \quad \mathbf{K}^J \mathbf{U}_{\text{RB}} = \mathbf{0}. \quad (38)$$

The remainder of the derivation will be presented only for the stiffness matrix, however, all equations apply to both damping matrices  $\mathbf{C}^J$  and  $\mathbf{D}^J$  as well. Pre-multiplying Eq. (38) by the identity  $\mathbf{I}$  and performing vectorization leads to:

$$(\mathbf{U}_{\text{RB}}^\top \otimes \mathbf{I}) \text{vec}(\mathbf{K}^J) = \mathbf{0}. \quad (39)$$

The symmetry of  $\mathbf{K}^J$  is taken into consideration by applying Eq. (24):

$$(\mathbf{U}_{\text{RB}}^\top \otimes \mathbf{I}) \text{Lvech}(\mathbf{K}^J) = \mathbf{0} \quad \Leftrightarrow \quad (\mathbf{U}_{\text{RB}}^\top \otimes \mathbf{I}) \mathbf{L} \mathbf{k}^J = \mathbf{0}. \quad (40)$$

All feasible solutions for  $\mathbf{c}^J$ ,  $\mathbf{d}^J$ , and  $\mathbf{k}^J$  must therefore span the null space of  $(\mathbf{U}_{\text{RB}}^\top \otimes \mathbf{I}) \mathbf{L}$ , i.e.:

$$\mathbf{k}^J \in \text{Null}((\mathbf{U}_{\text{RB}}^\top \otimes \mathbf{I}) \mathbf{L}). \quad (41)$$

Let  $\mathbf{V}$  denote the matrix containing all basis vectors of  $\text{Null}((\mathbf{U}_{\text{RB}}^\top \otimes \mathbf{I}) \mathbf{L})$  in its columns. The solutions for  $\mathbf{c}^J$ ,  $\mathbf{d}^J$ , and  $\mathbf{k}^J$  can therefore be expressed as a superposition of the null space basis vectors:

$$\mathbf{c}^J = \mathbf{V} \tilde{\mathbf{c}}^J, \quad \mathbf{d}^J = \mathbf{V} \tilde{\mathbf{d}}^J, \quad \mathbf{k}^J = \mathbf{V} \tilde{\mathbf{k}}^J, \quad \text{where} \quad \mathbf{V} \triangleq \text{Null}((\mathbf{U}_{\text{RB}}^\top \otimes \mathbf{I}) \mathbf{L}). \quad (42)$$

Taking Eq. (42) into account, Eq. (25) can be rewritten as:

$$\mathbf{A} \mathbf{V}_p \tilde{\mathbf{p}} = \mathbf{y} \quad \Leftrightarrow \quad \tilde{\mathbf{A}} \tilde{\mathbf{p}} = \mathbf{y}, \quad (43)$$

where

$$\mathbf{V}_p = \begin{bmatrix} \mathbf{I} & & & \\ & \mathbf{V} & & \\ & & \mathbf{V} & \\ & & & \mathbf{V} \end{bmatrix} \quad \text{and} \quad \tilde{\mathbf{p}} = \begin{bmatrix} \mathbf{m}^J \\ \tilde{\mathbf{c}}^J \\ \tilde{\mathbf{d}}^J \\ \tilde{\mathbf{k}}^J \end{bmatrix}. \quad (44)$$

Both  $\mathbf{y}$  and  $\mathbf{A}$  are frequency-dependent, while  $\mathbf{V}_p$  and  $\tilde{\mathbf{p}}$  are frequency-independent. Eq. (43) can be written at individual frequency lines, which can be gathered in a single equation:

$$\begin{bmatrix} \mathbf{A}(\omega_1) \mathbf{V}_p \\ \vdots \\ \mathbf{A}(\omega_N) \mathbf{V}_p \end{bmatrix} \tilde{\mathbf{p}} = \begin{bmatrix} \mathbf{y}(\omega_1) \\ \vdots \\ \mathbf{y}(\omega_N) \end{bmatrix} \quad \Leftrightarrow \quad \tilde{\mathbf{A}}_\Omega \tilde{\mathbf{p}} = \mathbf{y}_\Omega, \quad (45)$$

Again, since  $\tilde{\mathbf{p}}$  is real, both  $\tilde{\mathbf{A}}_\Omega$  and  $\mathbf{y}_\Omega$  can be split into real and imaginary parts to obtain a real solution for  $\tilde{\mathbf{p}}$ :

$$\begin{bmatrix} \text{Re}(\tilde{\mathbf{A}}_\Omega) \\ \text{Im}(\tilde{\mathbf{A}}_\Omega) \end{bmatrix} \tilde{\mathbf{p}} = \begin{bmatrix} \text{Re}(\mathbf{y}_\Omega) \\ \text{Im}(\mathbf{y}_\Omega) \end{bmatrix}. \quad (46)$$

Solving Eq. (46) in a least-squares sense allows to identify the parameters of the joint with both reciprocity of the system matrices and free-boundary conditions taken into account. Finally, the vectorized system matrices are calculated as:

$$\text{vec}(\mathbf{P}) = \mathbf{L}_p \mathbf{V}_p \tilde{\mathbf{p}}. \quad (47)$$

Taking Eq. (42) into account will be referred to as rigid-body-mode (RBM) constraints and can be interpreted as a generalization of the joint identification methods which use the linear springs formulation by including cross coupling between the adjacent joint DoFs without violating the rank-deficiency of the stiffness and damping matrices.

### 3.3. Sparse regression

Identifying the joint parameters is inherently subject to experimental errors, which pollute the identification results. The LS procedure can therefore be prone to overfitting, as it can identify some parameters as significant only to reduce the difference between the uncoupled and coupled response models. Experimental errors alter the discrepancy between the uncoupled and coupled states, while LS finds the best-fitting joint parameters regardless of the experimental errors. Therefore, it can be beneficial to perform sparse regression to eliminate some of the terms in the system matrices, which may be present due to inaccurate measurements. This work considers LASSO as the sparse regression method of choice. Considering a system of linear equations  $\mathbf{X}\boldsymbol{\beta} = \mathbf{y}$ , the LASSO solution  $\hat{\boldsymbol{\beta}}$  is found by solving Eq. (48):

$$\hat{\boldsymbol{\beta}} = \underset{\boldsymbol{\beta}}{\text{argmin}} (\|\mathbf{y} - \mathbf{X}\boldsymbol{\beta}\|_2^2 + \lambda \|\boldsymbol{\beta}\|_1), \quad (48)$$

where  $\lambda \|\boldsymbol{\beta}\|_1$  is the penalty term responsible for variable selection, with  $\lambda$  determining the penalty strength. Applying LASSO when RBM constraints are considered (Eq. (45)) may however not be beneficial, as the terms in  $\tilde{\mathbf{c}}^j$ ,  $\tilde{\mathbf{d}}^j$  and  $\tilde{\mathbf{k}}^j$  represent the coefficients for the superposition of columns in  $\mathbf{V}$ , and not the terms in the system matrices, as seen from Eq. (42). Since the aim is to promote sparsity of the system matrices, LASSO should be applied directly to the terms in the system matrices in  $\mathbf{p}$  (Eq. (26)). To make LASSO compatible with RBM constraints, LASSO is utilized exclusively to perform variable selection (i.e. to promote a sparse solution) in Eq. (25), similar to the application in [44]. The parameters eliminated by LASSO are therefore removed from the identification procedure. RBM constraints are subsequently modified to account for the eliminated parameters. By performing LASSO only for variable selection, application of RBM constraints is permitted, allowing to enforce rank deficiency of the sparse joint model. A flowchart describing the application of LASSO only for variable selection is provided in Fig. 2.

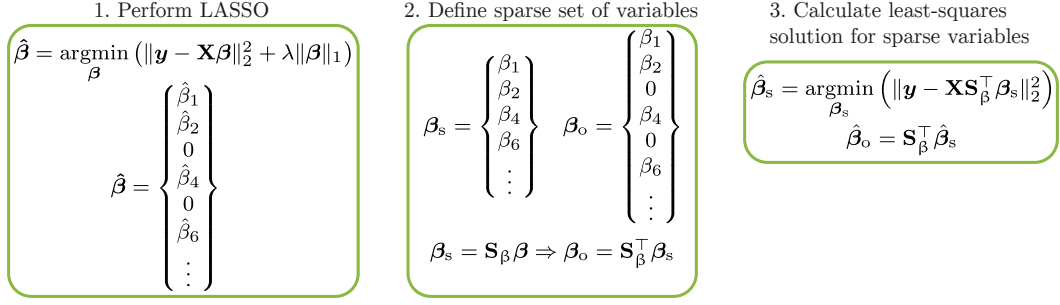


Figure 2: Flowchart describing the use of LASSO to perform variable selection only.  $\mathbf{S}_\beta$  denotes the selection matrix, which selects the sparse set of variables  $\beta_s$  from the set of all variables  $\beta$ , and  $\beta_o$  denotes the dense representation of the sparse variables  $\beta_s$ .

Applying LASSO to the set of all parameters  $\mathbf{p}$  can however be problematic, as FRFs are sensitive to damping only at frequencies in the vicinity of resonance peaks. Therefore, LASSO tends to remove a majority of damping parameters, leading to underestimated joint damping. It is therefore beneficial to search for a sparse solution only among the mass and stiffness parameters  $\mathbf{m}^J$  and  $\mathbf{k}^J$ . The columns of  $\mathbf{A}$  and terms in  $\mathbf{p}$  in Eq. (25) can be rearranged as follows:

$$\begin{bmatrix} \mathbf{A}_{\text{mk}} & \mathbf{A}_{\text{cd}} \end{bmatrix} \begin{bmatrix} \mathbf{p}_{\text{mk}} \\ \mathbf{p}_{\text{cd}} \end{bmatrix} = \mathbf{y}, \quad \text{with} \quad \mathbf{p}_{\text{mk}} \triangleq \begin{bmatrix} \mathbf{m}^J \\ \mathbf{k}^J \end{bmatrix} \quad \text{and} \quad \mathbf{p}_{\text{cd}} \triangleq \begin{bmatrix} \mathbf{c}^J \\ \mathbf{d}^J \end{bmatrix}. \quad (49)$$

Applying LASSO only to the subset  $\mathbf{p}_{\text{mk}}$  of all parameters is defined as:

$$\hat{\mathbf{p}}_{\text{mk}}, \hat{\mathbf{p}}_{\text{cd}} = \underset{\mathbf{p}_{\text{mk}}, \mathbf{p}_{\text{cd}}}{\operatorname{argmin}} \left( \|\mathbf{y} - \mathbf{A}_{\text{mk}}\mathbf{p}_{\text{mk}} - \mathbf{A}_{\text{cd}}\mathbf{p}_{\text{cd}}\|_2^2 + \lambda \|\mathbf{p}_{\text{mk}}\|_1 \right). \quad (50)$$

The problem in Eq. (50) can be reformulated to an ordinary LASSO problem as in Eq. (48)<sup>3</sup>:

$$\hat{\mathbf{p}}_{\text{mk}} = \underset{\mathbf{p}_{\text{mk}}}{\operatorname{argmin}} \left( \|\tilde{\mathbf{y}} - \tilde{\mathbf{A}}_{\text{mk}}\mathbf{p}_{\text{mk}}\|_2^2 + \lambda \|\mathbf{p}_{\text{mk}}\|_1 \right), \quad (51)$$

where

$$\tilde{\mathbf{y}} \triangleq (\mathbf{I} - \mathbf{H}_{\text{cd}}) \mathbf{y}, \quad \tilde{\mathbf{A}}_{\text{mk}} \triangleq (\mathbf{I} - \mathbf{H}_{\text{cd}}) \mathbf{A}_{\text{mk}}, \quad \text{and} \quad \mathbf{H}_{\text{cd}} \triangleq \mathbf{A}_{\text{cd}} (\mathbf{A}_{\text{cd}}^\top \mathbf{A}_{\text{cd}})^{-1} \mathbf{A}_{\text{cd}}^\top. \quad (52)$$

Although solving Eq. (51) provides solutions for  $\mathbf{m}^J$  and  $\mathbf{k}^J$ , LASSO is only used as a sparsity indicator to perform subset selection. Denoting the selected (nonzero) parameters as  $\mathbf{m}_s^J$  and  $\mathbf{k}_s^J$ , selection matrices  $\mathbf{S}_m$  and  $\mathbf{S}_k$  are constructed such that:

$$\mathbf{m}_s^J = \mathbf{S}_m \mathbf{m}^J, \quad (53a)$$

$$\mathbf{k}_s^J = \mathbf{S}_k \mathbf{k}^J. \quad (53b)$$

Matrices  $\mathbf{S}_m$  and  $\mathbf{S}_k$  select the nonzero elements from the original variables  $\mathbf{m}^J$  and  $\mathbf{k}^J$ . The matrices are constructed by taking the identity matrix and removing the rows corresponding to the nullified parameters. Matrices  $\mathbf{S}_m$  and  $\mathbf{S}_k$  are semi-orthogonal, as  $\mathbf{S}_m \mathbf{S}_m^\top = \mathbf{I}$  and  $\mathbf{S}_k \mathbf{S}_k^\top = \mathbf{I}$ . Eqs. (53a) and (53b) are pre-multiplied by  $\mathbf{S}_m^\top$  and  $\mathbf{S}_k^\top$ :

$$\mathbf{S}_m^\top \mathbf{m}_s^J = \mathbf{S}_m^\top \mathbf{S}_m \mathbf{m}^J, \quad (54a)$$

$$\mathbf{S}_k^\top \mathbf{k}_s^J = \mathbf{S}_k^\top \mathbf{S}_k \mathbf{k}^J. \quad (54b)$$

<sup>3</sup>The interested reader is referred to Appendix A, where the problem of LASSO applied to only a subset of all variables is derived to a reformulated ordinary LASSO problem.

Since  $\mathbf{S}_m$  and  $\mathbf{S}_k$  are semi-orthogonal<sup>4</sup>, the products  $\mathbf{S}_m^\top \mathbf{S}_m$  and  $\mathbf{S}_k^\top \mathbf{S}_k$  represent the orthogonal projection onto the row space of  $\mathbf{S}_m$  and  $\mathbf{S}_k$ , respectively. As the row spaces of these matrices do not contain any nonzero terms corresponding to the parameters eliminated by LASSO,  $\mathbf{S}_m^\top \mathbf{S}_m$  and  $\mathbf{S}_k^\top \mathbf{S}_k$  set these parameters in  $\mathbf{m}^J$  and  $\mathbf{k}^J$  to zero via orthogonal projection and retain the nonzero terms unchanged, effectively sparsifying  $\mathbf{m}^J$  and  $\mathbf{k}^J$ . Their sparse representations are denoted by  $\mathbf{m}_o^J$  and  $\mathbf{k}_o^J$ , respectively, which are calculated as:

$$\mathbf{m}_o^J = \mathbf{S}_m^\top \mathbf{S}_m \mathbf{m}^J = \mathbf{S}_m^\top \mathbf{m}_s^J, \quad (55a)$$

$$\mathbf{k}_o^J = \mathbf{S}_k^\top \mathbf{S}_k \mathbf{k}^J = \mathbf{S}_k^\top \mathbf{k}_s^J. \quad (55b)$$

The sparsity is accounted for by replacing  $\mathbf{m}^J$  and  $\mathbf{k}^J$  in Eq. (25) with  $\mathbf{S}_m^\top \mathbf{m}_s^J$  and  $\mathbf{S}_k^\top \mathbf{k}_s^J$ , respectively:

$$\mathbf{A} \mathbf{S}^\top \mathbf{p}_s = \mathbf{y}, \quad (56)$$

where

$$\mathbf{S}^\top \triangleq \begin{bmatrix} \mathbf{S}_m^\top & & \\ & \mathbf{I} & \\ & & \mathbf{I} \\ & & & \mathbf{S}_k^\top \end{bmatrix} \quad \text{and} \quad \mathbf{p}_s \triangleq \begin{bmatrix} \mathbf{m}_s^J \\ \mathbf{c}^J \\ \mathbf{d}^J \\ \mathbf{k}_s^J \end{bmatrix}. \quad (57)$$

After promoting sparsity of  $\mathbf{m}^J$  and  $\mathbf{k}^J$ , the rigid-body motion should be taken into consideration. Both  $\mathbf{c}^J$  and  $\mathbf{d}^J$  remain dense, therefore, the transformation changes only for the stiffness parameters, rewriting Eqs. (40) and (41) as:

$$(\mathbf{U}_{RB}^\top \otimes \mathbf{I}) \mathbf{L} \mathbf{S}_k^\top \mathbf{k}_s^J = \mathbf{0} \quad \Leftrightarrow \quad \mathbf{k}_s^J \in \text{Null}((\mathbf{U}_{RB}^\top \otimes \mathbf{I}) \mathbf{L} \mathbf{S}_k^\top). \quad (58)$$

The matrix containing all basis vectors of  $\text{Null}((\mathbf{U}_{RB}^\top \otimes \mathbf{I}) \mathbf{L} \mathbf{S}_k^\top)$  in its columns is denoted as  $\mathbf{V}_k$ , which complies with the rigid-body motion and accounts for the symmetry and sparsity of  $\mathbf{K}^J$ . Eq. (42) is adjusted to account for the sparse stiffness parameters:

$$\mathbf{k}_s^J = \mathbf{V}_k \tilde{\mathbf{k}}_s^J, \quad \text{where} \quad \mathbf{V}_k \triangleq \text{Null}((\mathbf{U}_{RB}^\top \otimes \mathbf{I}) \mathbf{L} \mathbf{S}_k^\top). \quad (59)$$

Inserting Eqs. (42) and (59) into Eq. (56) yields:

$$\mathbf{A} \mathbf{S}^\top \mathbf{V}_{ps} \tilde{\mathbf{p}}_s = \mathbf{y} \quad \Leftrightarrow \quad \tilde{\mathbf{A}}_s \tilde{\mathbf{p}}_s = \mathbf{y}, \quad (60)$$

where

$$\mathbf{V}_{ps} = \begin{bmatrix} \mathbf{I} & & & \\ & \mathbf{V} & & \\ & & \mathbf{V} & \\ & & & \mathbf{V}_k \end{bmatrix} \quad \text{and} \quad \tilde{\mathbf{p}}_s = \begin{bmatrix} \mathbf{m}_s^J \\ \tilde{\mathbf{c}}^J \\ \tilde{\mathbf{d}}^J \\ \tilde{\mathbf{k}}_s^J \end{bmatrix}. \quad (61)$$

Again, Eq. (60) can be written at individual frequency lines and combined into a single equation:

$$\begin{bmatrix} \mathbf{A}(\omega_1) \mathbf{S}^\top \mathbf{V}_{ps} \\ \vdots \\ \mathbf{A}(\omega_N) \mathbf{S}^\top \mathbf{V}_{ps} \end{bmatrix} \tilde{\mathbf{p}}_s = \begin{bmatrix} \mathbf{y}(\omega_1) \\ \vdots \\ \mathbf{y}(\omega_N) \end{bmatrix} \quad \Leftrightarrow \quad \tilde{\mathbf{A}}_{s\Omega} \tilde{\mathbf{p}}_s = \mathbf{y}_\Omega. \quad (62)$$

Both  $\tilde{\mathbf{A}}_{s\Omega}$  and  $\mathbf{y}_\Omega$  are split into real and imaginary parts, allowing to calculate the real least-squares solution of Eq. (62):

$$\tilde{\mathbf{p}}_s = \begin{bmatrix} \text{Re}(\tilde{\mathbf{A}}_{s\Omega}) \\ \text{Im}(\tilde{\mathbf{A}}_{s\Omega}) \end{bmatrix}^+ \begin{bmatrix} \text{Re}(\mathbf{y}_\Omega) \\ \text{Im}(\mathbf{y}_\Omega) \end{bmatrix}. \quad (63)$$

Finally, the vectorized system matrices can be calculated:

$$\text{vec}(\mathbf{P}) = \mathbf{L}_p \mathbf{S}^\top \mathbf{V}_{ps} \tilde{\mathbf{p}}_s. \quad (64)$$

---

<sup>4</sup>Matrices  $\mathbf{S}_m$  and  $\mathbf{S}_k$  are semi-orthogonal, as they are not square, however,  $\mathbf{S}_m \mathbf{S}_m^\top = \mathbf{I}$  and  $\mathbf{S}_k \mathbf{S}_k^\top = \mathbf{I}$ .

### 3.4. Excitation direction updating

Experimentally obtaining FRFs is inherently subject to errors. Consistent locations and directions of excitations and measured responses are especially important when applying the VPT to model the interface, as the location and direction errors propagate through the transformation [41]. To understand the influence of locations and directions of excitation and response DoFs, the following subsection briefly explains the basic formulation of the VPT.

#### 3.4.1. Virtual point transformation

Performing coupling and decoupling operations in DS relies on the ability to establish the constraints of interface displacement compatibility and interface force equilibrium. A prerequisite to establishing both types of constraints are collocated DoFs on the adjacent sides of the interface, which is difficult to achieve in an experimental environment. Replicating excitation locations can be challenging when the interface is not easily accessible for measurements. Even if measurement locations could be replicated, directly coupling too many interface DoFs can result in unwanted stiffening of the interface, leading to an ill-conditioned substructuring problem and spurious peaks in the estimated vibration response [45].

The motion at the interface can often be sufficiently described as a superposition of selected interface deformation modes (IDMs). For point-like connections, where the interface locally exhibits rigid behavior, six rigid-body IDMs are sufficient to approximate arbitrary interface motion. The VPT allows to transform the translational DoFs measured in the proximity of the interface to a six-DoF virtual point (VP). Its location can be chosen arbitrarily, therefore, collocated DoFs on either side of the interface can be easily obtained [19].

The derivation of VPT is facilitated by Fig. 3. The VPT can be understood as a reduction of measured DoFs by means of geometric transformation, which is applied separately to excitation and response DoFs. The following derivation will only consider rigid-body IDMs, however, flexible interface motion can also be accounted for [46]. Assuming the VP responses  $\mathbf{q}^{\text{VP}} = [q_x \ q_y \ q_z \ q_{\theta x} \ q_{\theta y} \ q_{\theta z}]^\top$  are known, a single measured response  $u^h$  can be expressed as:

$$u^h = \begin{bmatrix} \mathbf{e}^h^\top & (\mathbf{r}^h \times \mathbf{e}^h)^\top \end{bmatrix} \mathbf{q}^{\text{VP}} + \mu^h \Leftrightarrow u^h = \mathbf{R}_u^h \mathbf{q}^{\text{VP}} + \mu^h, \quad (65)$$

where  $\mathbf{e}^h$  and  $\mathbf{r}^h$  are respectively the direction and relative location vectors of displacement  $u^h$ , as illustrated by Fig. 3, and  $\mu^h$  accounts for any discrepancy between the transformed VP response  $\mathbf{R}_u^h \mathbf{q}^{\text{VP}}$  and the measured response  $u^h$ . All measured responses  $\mathbf{u}$  are expressed in terms of the VP responses  $\mathbf{q}^{\text{VP}}$  as:

$$\mathbf{u} = \mathbf{R}_u \mathbf{q}^{\text{VP}} + \boldsymbol{\mu}, \quad (66)$$

where  $\mathbf{R}_u$  is the IDM matrix obtained by vertically stacking  $\mathbf{R}_u^h$  and  $\boldsymbol{\mu}$  accounts for any residual motion in  $\mathbf{u}$  outside the column space of  $\mathbf{R}_u$ . The number of VP responses in  $\mathbf{q}^{\text{VP}}$  should not exceed the number of measured responses in  $\mathbf{u}$  to ensure the VP responses are mutually independent. In practice, Eq. (66) should be overdetermined to reduce the effect of measurement errors. The least-squares solution to Eq. (66) can be found by minimizing  $\boldsymbol{\mu}^\top \boldsymbol{\mu}$ :

$$\mathbf{q}^{\text{VP}} = \mathbf{T}_u \mathbf{u}, \quad \text{where} \quad \mathbf{T}_u = (\mathbf{R}_u^\top \mathbf{R}_u)^{-1} \mathbf{R}_u^\top. \quad (67)$$

The matrix  $\mathbf{T}_u$  is known as the left inverse of  $\mathbf{R}_u$ , solving Eq. (66) in a least-squares sense.

In contrast to responses, the VP loads  $\mathbf{m}^{\text{VP}} = [m_x \ m_y \ m_z \ m_{\theta x} \ m_{\theta y} \ m_{\theta z}]^\top$  represent the resultant force due to the applied forces  $\mathbf{f}$ . If a single force  $f^k$  is applied, the VP loads are calculated as:

$$\mathbf{m}^{\text{VP}} = \begin{bmatrix} \mathbf{e}^k \\ \mathbf{r}^k \times \mathbf{e}^k \end{bmatrix} f^k \Leftrightarrow \mathbf{m}^{\text{VP}} = \mathbf{R}_f^k f^k, \quad (68)$$

where  $\mathbf{e}^k$  and  $\mathbf{r}^k$  are respectively the direction and relative location vectors of excitation  $f^k$ , as illustrated by Fig. 3. The VP loads due to all applied forces are calculated by horizontally stacking  $\mathbf{R}_f^k$ :

$$\mathbf{m}^{\text{VP}} = \mathbf{R}_f^\top \mathbf{f}. \quad (69)$$

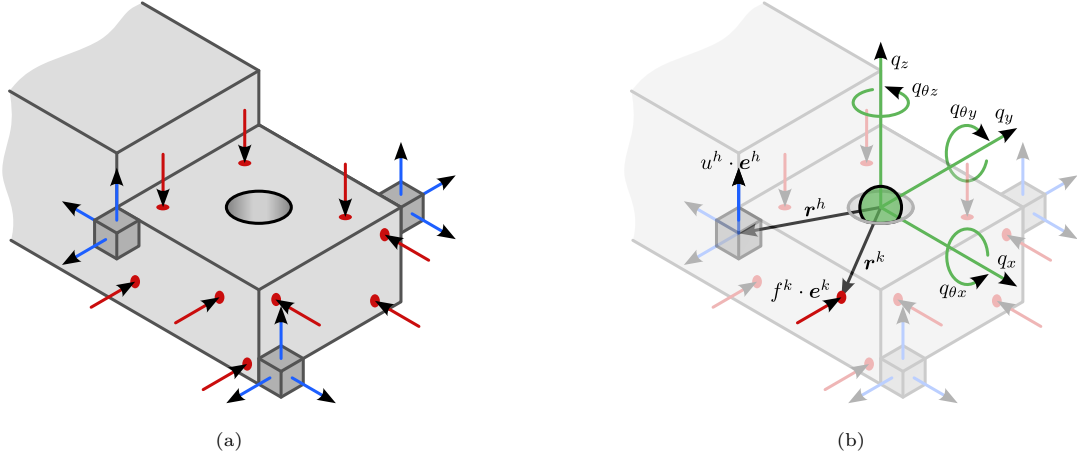


Figure 3: Representation of the interface as a virtual point: (a) interface excitation & response measurements, (b) transformation to VP DoFs. Blue (—), red (—), and green (—) colors indicate the response, excitation, and VP DoFs, respectively.

Applying the VPT to excitations requires expressing the applied forces  $\mathbf{f}$  in terms of the VP loads  $\mathbf{m}^{\text{VP}}$ . To describe an arbitrary VP load, the number of forces in  $\mathbf{f}$  should at least match the number of VP loads. By ensuring the number of forces in  $\mathbf{f}$  exceeds the number of VP loads, Eq. (69) is underdetermined, reducing the effects of measurement errors. The forces  $\mathbf{f}$  in Eq. (3) should be replaced by the least-norm solution of Eq. (69), denoted by  $\hat{\mathbf{f}}$ , to ensure the interface is excited such that the loads not described by the IDMs in  $\mathbf{R}_f^\top$  are minimized:

$$\hat{\mathbf{f}} = \mathbf{T}_f^\top \mathbf{m}^{\text{VP}}, \quad \text{where} \quad \mathbf{T}_f^\top = \mathbf{R}_f (\mathbf{R}_f^\top \mathbf{R}_f)^{-1}. \quad (70)$$

The matrix  $\mathbf{T}_f^\top$  is known as the right-inverse of  $\mathbf{R}_f^\top$ , solving Eq. (69) in a least-norm sense. Finally, the measured admittance  $\mathbf{Y}$  is transformed to VP admittance  $\mathbf{Y}_{\text{qm}}$  by substituting the measured DoFs with VP DoFs using Eqs. (67) and (70), as described in [19]:

$$\mathbf{u} = \mathbf{Y} \mathbf{f} \quad \Rightarrow \quad \mathbf{q}^{\text{VP}} = \mathbf{T}_u \mathbf{Y} \mathbf{T}_f^\top \mathbf{m}^{\text{VP}} = \mathbf{Y}_{\text{qm}} \mathbf{m}^{\text{VP}}. \quad (71)$$

A transformation from VP DoFs to the measured DoFs can also be performed, which calculates the filtered admittance:

$$\hat{\mathbf{u}} = \mathbf{R}_u \mathbf{Y}_{\text{qm}} \mathbf{R}_f^\top \hat{\mathbf{f}} = \mathbf{R}_u \mathbf{T}_u \mathbf{Y} \mathbf{T}_f^\top \mathbf{R}_f^\top \hat{\mathbf{f}} = \mathbf{F}_u \mathbf{Y} \mathbf{F}_f \hat{\mathbf{f}} = \hat{\mathbf{Y}} \hat{\mathbf{f}}, \quad (72)$$

where  $\mathbf{F}_u$  and  $\mathbf{F}_f$  are the response and excitation projection matrices filtering out any motion from  $\mathbf{Y}$  which cannot be described by the selected IDMs, resulting in the filtered admittance matrix  $\hat{\mathbf{Y}}$ .

Consistent VPT requires both selecting the appropriate IDMs, as well as ensuring the individual terms in the IDM matrices are consistent with the true locations and directions of response and excitation DoFs. Assuming the selected IDMs are sufficient to fully describe the interface motion, the VPT consistency is predominantly subject to the consistency of excitation and response locations and directions. If the VPT is used to model the interface DoFs of the joint, the joint model accuracy is influenced by the VPT consistency, which is in turn related to the locations and directions of the measured excitation and response DoFs. By carefully mounting sensors on the structure, the main contribution to uncertainty in the VPT can be attributed to excitation location and direction errors. The consistency of force DoFs may be improved by fine-tuning the locations and directions in the IDM matrices, as discussed in [47]. In case of a large enough interface, the main source of uncertainty lies in the excitation direction inaccuracy, as the relative location error decreases with distance from the VP. Furthermore, all VP loads are influenced by the excitation directions, while only the rotational VP loads are influenced by the excitation locations. Therefore, excitation direction uncertainty is arguably more influential.

An optimization approach for updating excitation and response locations and directions was proposed in [48], where a cost function was defined by considering VP rigidness, reciprocity, and passivity. In this work,

a similar idea is explored, focusing only on updating excitation directions. Instead of a cost function-based optimization procedure, an iterative updating approach is proposed, relying on enforcing VP reciprocity and calculating the excitation directions which minimize the difference between the measured and filtered admittance. In the following, the proposed algorithm for updating excitation directions is presented.

#### 3.4.2. Updating excitation directions

Inconsistent excitation directions lead to errors in VPT due to the excitation directions considered in the VPT deviating from the true directions. Regardless of appropriately selecting IDMs, this leads to increased discrepancy between the measured and filtered FRFs. The aim of excitation direction updating is to find the true excitation directions, thereby decreasing the filtering effect. The updating procedure relies on iteratively applying the VPT, enforcing VP admittance reciprocity, and applying an inverse transformation with the excitation directions considered as unknown variables within the inverse transformation. This procedure is briefly illustrated in Fig. 4, followed by a detailed description of the updating algorithm.

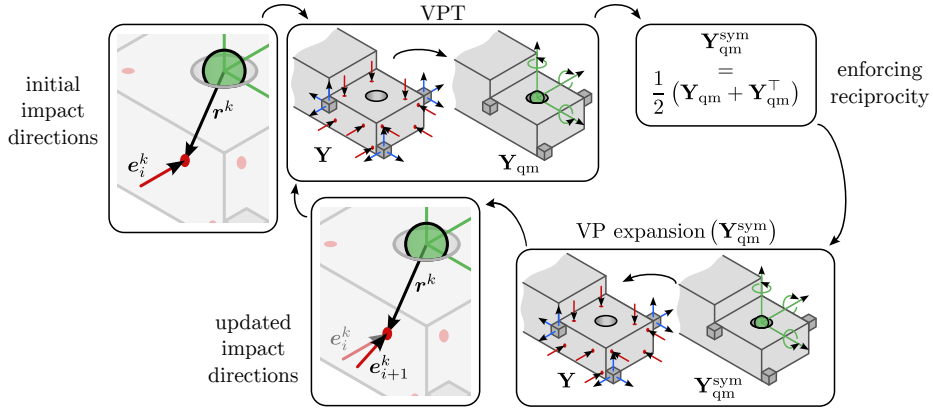


Figure 4: Excitation direction updating algorithm.

To update excitation directions, each column  $\mathbf{R}_f^{k\top}$  in  $\mathbf{R}_f^\top$  is written as a transformation of excitation direction  $\mathbf{e}^k$ :

$$\mathbf{R}_f^{k\top} = \begin{bmatrix} \mathbf{e}^k \\ \mathbf{r}^k \times \mathbf{e}^k \end{bmatrix} = \begin{bmatrix} 1 & 0 & 0 \\ 0 & 1 & 0 \\ 0 & 0 & 1 \\ 0 & -r_z^k & r_y^k \\ r_z^k & 0 & -r_x^k \\ -r_y^k & r_x^k & 0 \end{bmatrix} \begin{bmatrix} e_x^k \\ e_y^k \\ e_z^k \end{bmatrix} = \bar{\mathbf{R}}_f^{k\top} \mathbf{e}^k. \quad (73)$$

The updating of excitation directions is conducted by iteratively performing the following sequence of steps:

1. Construct the matrix  $\mathbf{R}_{f,i}^\top$  using the directions  $\mathbf{e}_i^k$  from the  $i$ th iteration.
2. Calculate the VP admittance:

$$\mathbf{Y}_{\text{qm},i} = \mathbf{R}_u^+ \mathbf{Y} \mathbf{R}_{f,i}^{\top+}. \quad (74)$$

3. Enforce reciprocity by calculating the symmetric part of the VP admittance:

$$\mathbf{Y}_{\text{qm},i}^{\text{sym}} = \frac{1}{2} (\mathbf{Y}_{\text{qm},i} + \mathbf{Y}_{\text{qm},i}^\top). \quad (75)$$

4. Express each column of the filtered admittance using the symmetric matrix  $\mathbf{Y}_{\text{qm},i}^{\text{sym}}$  and excitation direction  $\mathbf{e}_i^k$  and denote the difference between each column of the measured and filtered admittance matrices as  $\delta_{i+1}^k$ :

$$\delta_{i+1}^k = \mathbf{R}_u \mathbf{Y}_{\text{qm},i}^{\text{sym}} \bar{\mathbf{R}}_f^{k\top} \mathbf{e}_{i+1}^k - \mathbf{y}^k, \quad (76)$$

where  $\mathbf{y}^k$  denotes the  $k$ th column of the measured admittance matrix  $\mathbf{Y}$ .

- Eq. (76) can be written for all available frequencies in the range where the selected IDMs are considered to be dominant. In addition, Eq. (76) can be pre-multiplied by a frequency-dependent weighting matrix  $\mathbf{W}(\omega)$  to make better use of the available information:

$$\begin{bmatrix} \vdots \\ \mathbf{W}(\omega_j) \bar{\boldsymbol{\delta}}_{i+1}^k(\omega_j) \\ \vdots \end{bmatrix} = \begin{bmatrix} \vdots \\ \mathbf{W}(\omega_j) \mathbf{R}_u \mathbf{Y}_{\text{qm},i}^{\text{sym}}(\omega_j) \bar{\mathbf{R}}_f^k{}^\top \\ \vdots \end{bmatrix} \mathbf{e}_{i+1}^k - \begin{bmatrix} \vdots \\ \mathbf{W}(\omega_j) \mathbf{y}^k(\omega_j) \\ \vdots \end{bmatrix}, \quad (77)$$

$\Leftrightarrow$

$$\bar{\boldsymbol{\delta}}_{i+1}^k = \mathbf{A}_i^k \mathbf{e}_{i+1}^k - \bar{\mathbf{y}}^k.$$

- Split  $\bar{\boldsymbol{\delta}}_{i+1}^k$ ,  $\mathbf{A}_i^k$ , and  $\bar{\mathbf{y}}^k$  into real and imaginary components and calculate the (weighted) least-squares solution of Eq. (77) for each impact direction  $\mathbf{e}_{i+1}^k$ :

$$\tilde{\mathbf{e}}_{i+1}^k = \begin{bmatrix} \text{Re}(\mathbf{A}_i^k) \\ \text{Im}(\mathbf{A}_i^k) \end{bmatrix}^+ \begin{bmatrix} \text{Re}(\bar{\mathbf{y}}^k) \\ \text{Im}(\bar{\mathbf{y}}^k) \end{bmatrix}. \quad (78)$$

- Normalize the least-squares solution for each excitation direction:

$$\mathbf{e}_{i+1}^k = \tilde{\mathbf{e}}_{i+1}^k / \|\tilde{\mathbf{e}}_{i+1}^k\|_2. \quad (79)$$

- Repeat steps 1–7 until a convergence criterion is satisfied:

$$1 - \frac{1}{N} \sum_{k=1}^N (\mathbf{e}_i^k)^\top \mathbf{e}_{i+1}^k \leq \varepsilon. \quad (80)$$

In step 3, the symmetric part of  $\mathbf{Y}_{\text{qm},i}$  is calculated, which facilitates finding the excitation directions that reduce the projection error of the symmetric matrix. Without enforcing the symmetry of  $\mathbf{Y}_{\text{qm},i}$ , the solution for  $\mathbf{e}_{i+1}^k$  minimizes only the projection error.

The excitation direction vectors in the VPT are assumed to be unit vectors, however, the least-squares method does not guarantee the solution to lie on the unit sphere. Eq. (77) could be solved by means of constrained optimization by defining the constraint  $\|\mathbf{e}_{i+1}^k\|_2 = 1$ , however, the least-squares approach combined with normalization achieves sufficient accuracy, therefore, alternative approaches were not tested. Lastly, a frequency-dependent weighting matrix  $\mathbf{W}(\omega)$  can be used to ensure the system of equations in (77) is not dominated by the terms at resonant frequencies due to the increased response amplitudes. In addition, the amplitudes of response at different DoFs may differ in orders of magnitude, which can also be accounted for by  $\mathbf{W}(\omega)$ .

A similar procedure was deduced for updating excitation locations, however, the updating algorithm had difficulties achieving converging results and is therefore not included in this work. Nevertheless, the excitation direction updating algorithm was able to successfully find the true excitation directions in numerical examples of noisy FRFs with both excitation direction and location uncertainty, as will be shown in Section 4. In the numerical study, the true excitation directions are known, allowing to evaluate the accuracy of the updated excitation directions. The chosen metric to describe the accuracy of direction  $\mathbf{e}_\star$  with respect to the true direction  $\mathbf{e}_{\text{true}}$  is their dot product:

$$f_{\text{accuracy}}(\mathbf{e}_\star, \mathbf{e}_{\text{true}}) = \mathbf{e}_\star^\top \mathbf{e}_{\text{true}}. \quad (81)$$

As both direction vectors are unit vectors, their dot product approaches 1 with increasing accuracy. Lastly, to assess the similarity of two FRFs, the coherence criterion is defined:

$$\text{coh}(Y, Y^{\text{ref}}) = \frac{(Y + Y^{\text{ref}})(\bar{Y} + \bar{Y}^{\text{ref}})}{2(Y\bar{Y} + Y^{\text{ref}}\bar{Y}^{\text{ref}})}, \quad (82)$$

where  $\bar{\star}$  denotes the complex conjugate of  $\star$ .

#### 4. Numerical study

Both the numerical and experimental studies are conducted on substructures of similar geometry. A resilient joint type is considered in both studies. Two assembled structures are assessed, namely the CJC and AJB structures. The CJC (cross-joint-cross) structure serves as a test rig for joint identification. The top and bottom cross structures have conforming geometry defined by several inclined planes to improve the channel and impact consistency.<sup>5</sup> The joint is first validated on the CJC structure, here referred to as onboard validation, i.e. validation is performed on the same set of substructures as the identification. Subsequently, validation is performed on the AJB structure, where the substructures A and B are connected by two identical joints. This will be referred to as cross validation, as the validation is performed on a set of substructures different from the substructures in the identification procedure.

The substructures comprising the CJC structure are shown in Fig. 5, while Fig. 6 depicts the substructures comprising the AJB structure. The red arrows represent excitations, while the transparent boxes represent triaxial accelerometers. Each of the two green spheres in Fig. 5b represents a single VP with six DoFs. Two VPs are used to construct the twelve joint DoFs. Applying the VPT, FRF synthesis, and visualization were facilitated by the open-source Python package pyFBS [49].

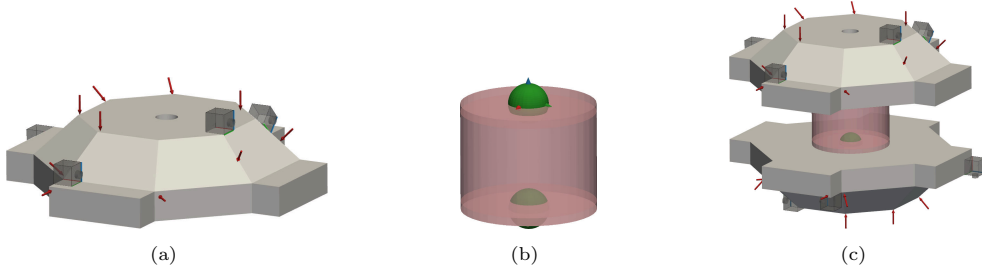


Figure 5: Identification and onboard validation substructures within numerical joint identification: (a) C, (b) J, (c) CJC.

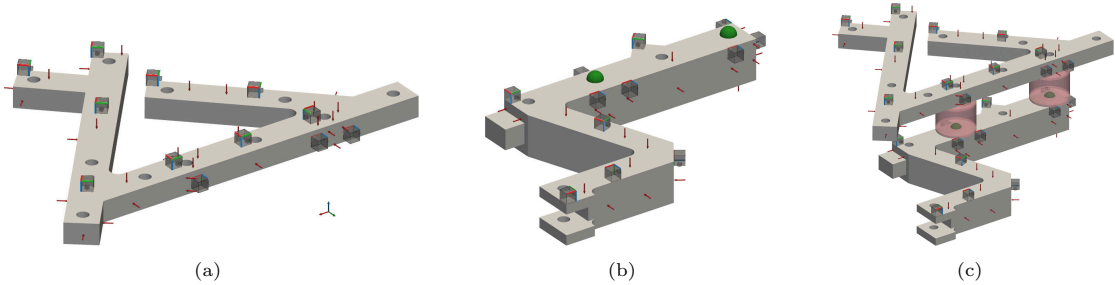


Figure 6: Cross validation substructures within numerical joint identification: (a) A, (b) B, (c) AJB.

The joint identification workflow is depicted in Fig. 7. Four modifications to the existing joint identification approaches are tested: direct or indirect parametrization, consideration of the joint rigid-body modes, least-squares or sparse regression, and original or updated excitation directions. As these methods are mutually independent, all possible combinations are tested, resulting in 16 distinct joint identification approaches. Both onboard and cross validation are performed to assess each approach.

<sup>5</sup>If the cross-coupling between the VP DoFs is low and excitation is performed in the direction of a VP DoF, some VP DoFs are expected to exhibit low response amplitudes, resulting in a low signal-to-noise ratio. Furthermore, a small deviation in excitation direction may significantly affect these responses, resulting in low impact consistency. Therefore, it is beneficial to deliberately excite as many VP DoFs as possible by choosing excitation directions not parallel to the VP DoFs. Similar reasoning can be applied to the positioning of measured responses.

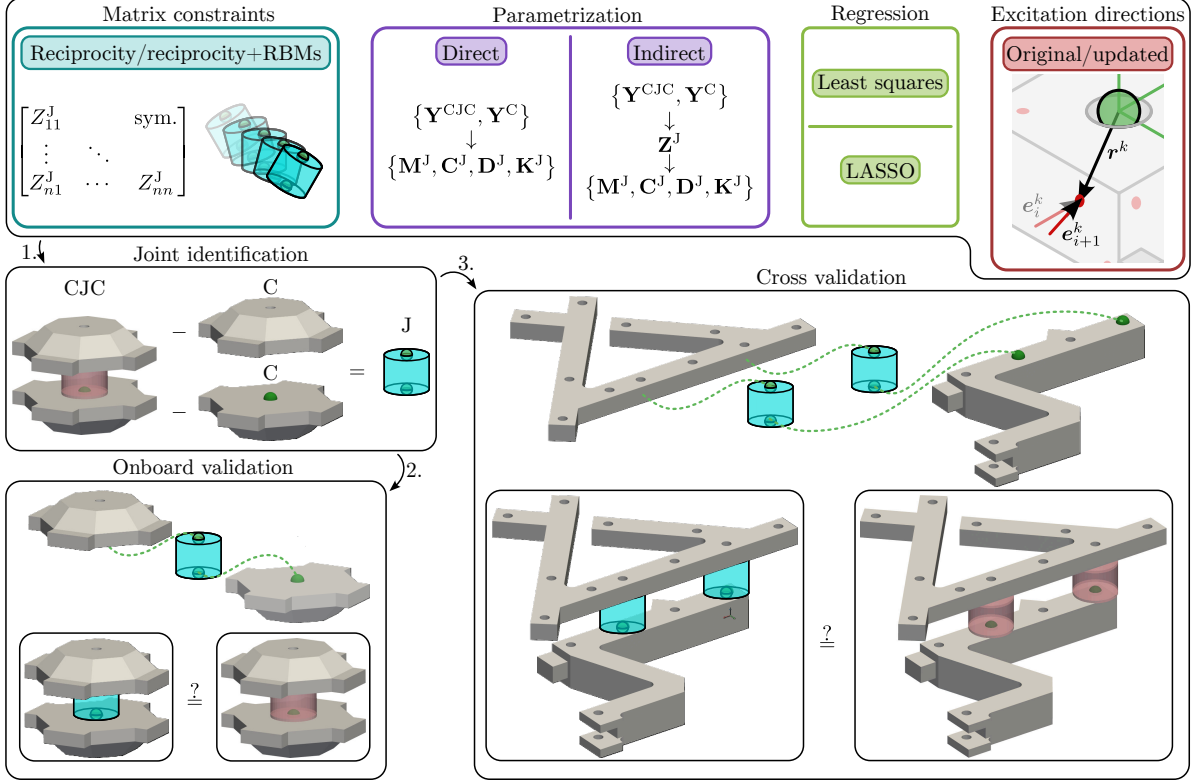


Figure 7: Joint identification workflow.

#### 4.1. Excitation direction updating validation

The excitation directions and locations considered for the VPT in the numerical study were slightly perturbed to replicate a realistic measurement environment. A random in-plane location error was added with a uniform distribution within a circle of 4 mm radius. Similarly, excitation directions were offset from the original directions by a direction error with uniform distribution on a spherical cap bounded by the polar angle (offset from the normal direction) of  $15^\circ$ . Random Gaussian noise with standard deviation of  $0.02 \text{ ms}^{-2}/\text{N}$  was added to both the real and imaginary parts of FRFs throughout the entire frequency range to approximate measurement noise.

A comparison of VP reciprocity before and after updating excitation directions is shown in Fig. 8, separately for substructure C and assembled CJC. The erroneous (non-updated) and updated directions are denoted as ERR and UP, respectively. An increase in reciprocity is observed after updating, which is promoted by the updating procedure, where VP reciprocity is enforced within each updating iteration. Since true excitation directions and locations are available in the numerical study, individual VP FRFs, obtained with erroneous and updated excitation directions, can also be compared to the VP FRFs with true excitation directions and locations. This is shown in Fig. 9, where ref., ERR, and UP refer to the VP FRFs calculated by considering the true, erroneous, and updated excitation directions, respectively. It can be seen from Fig. 9 that updating excitation directions improves the accuracy of the VP FRFs, which should improve the joint identification accuracy.

The accuracy of the excitation direction updating is assessed by evaluating the accuracy of the erroneous and updated excitation directions using Eq. (81), as the true excitation directions are also known. The accuracy of all excitations on both C and CJC structures are shown in Fig. 10. All excitation directions are significantly improved after updating.

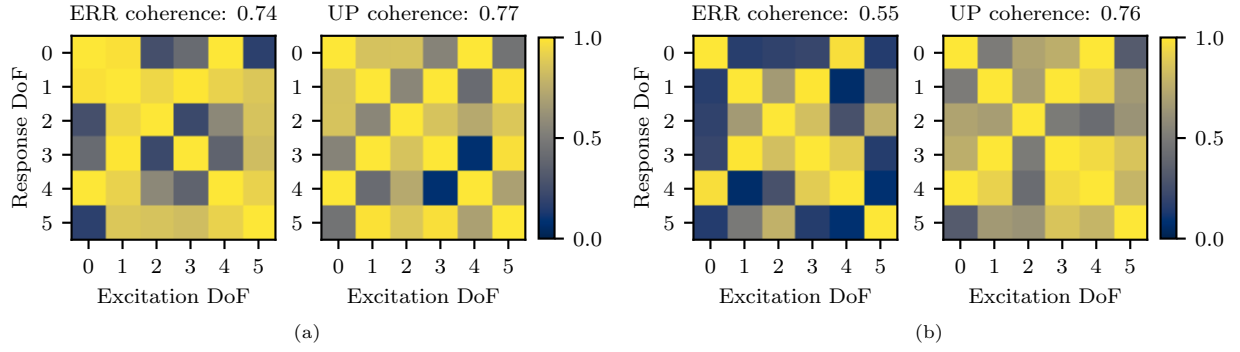


Figure 8: Reciprocity of the VP admittance matrix: (a) C, (b) CJC - upper VP.

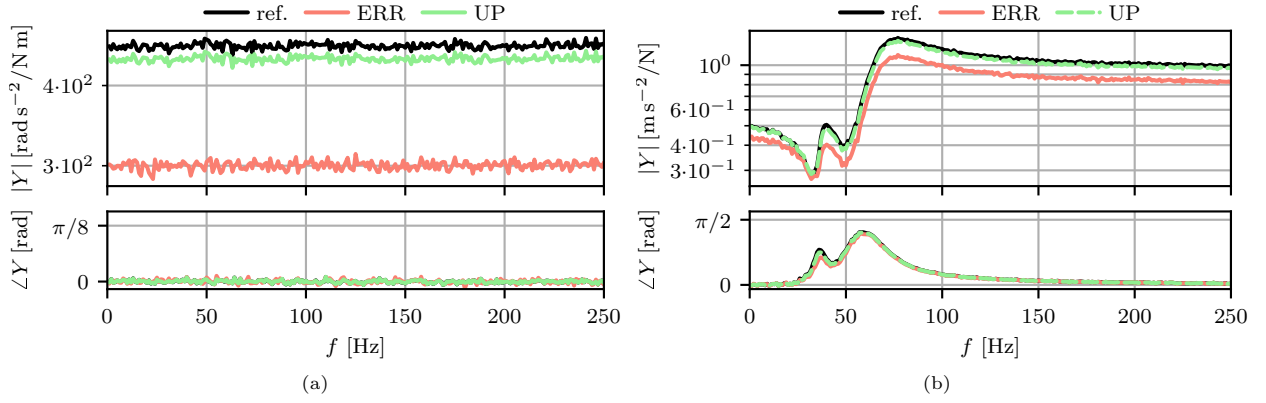


Figure 9: VP FRFs considering true, erroneous, and updated excitation directions: (a) substructure C, (b) structure CJC.

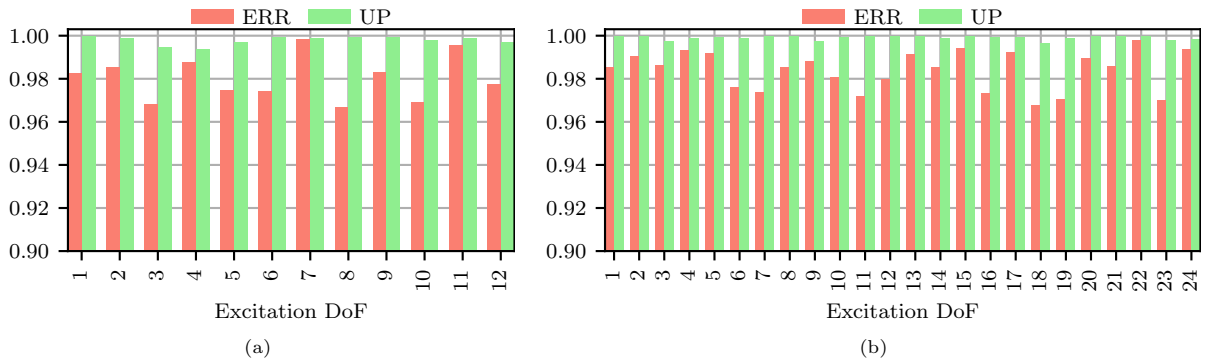


Figure 10: Accuracy of erroneous and updated excitation directions: (a) C, (b) CJC.

#### 4.2. Onboard validation

The individual identification approaches are first compared within onboard validation, where the dynamics of the CJC assembly, used for joint identification, are estimated by coupling the identified joint with the adjacent C substructures. In addition to the 16 parametrization approaches, joint identification is also performed in the frequency domain by applying Eq. (30) to obtain the joint's dynamic stiffness matrix. The frequency domain approach is denoted as FD, which directly identifies the dynamic stiffness matrix without subsequent parametrization.

The effect of RBM constraints is shown in Fig. 11. Neglecting RBM constraints results in a poor accuracy in the low frequency range (below 50 Hz), while no significant difference was observed at higher frequencies. This effect was consistently observed for all approaches, therefore, for the sake of brevity, the remaining results all comply with RBM constraints.

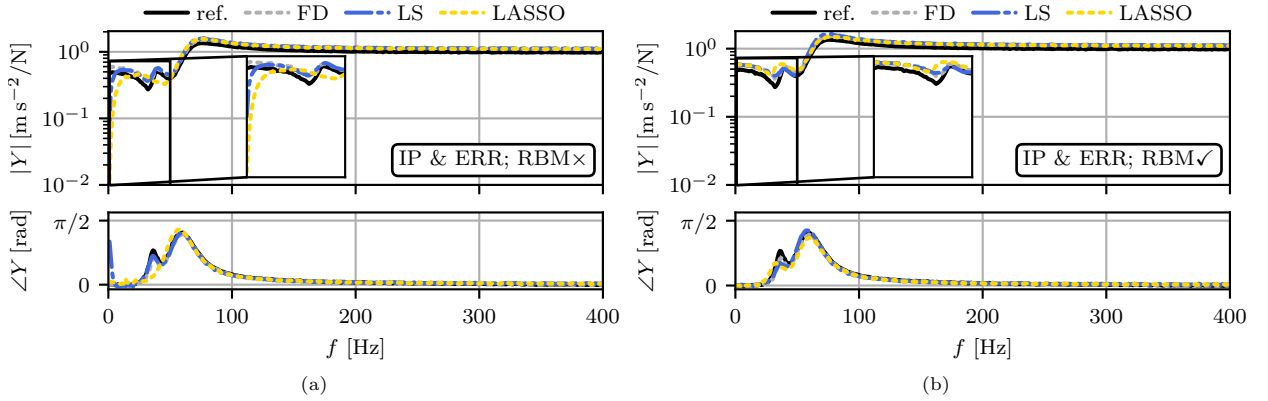


Figure 11: CJC FRFs obtained using indirect parametrization and erroneous excitation directions: (a) no RBM considerations, (b) joint matrices constrained by RBMs.

By considering RBM constraints, only eight distinct identification approaches are left, which vary in the regression approach (LS or LASSO), parametrization (DP or IP), and excitation directions (ERR or UP). Onboard validation results for all eight variants are shown in Fig. 12. All approaches are compared with the reference (true assembly) FRFs. The assembly FRFs are also estimated using the FD joint. Two distinct FD joint models are identified by individually considering the erroneous and the updated excitation directions. This allows to compare the parametrized joints with the FD joints while taking the excitation direction updating into account.

This paper aims to explore and compare different joint parametrization approaches, while the FD approach is not parametrized and characterizes the joint's properties per frequency. Therefore, it is not expected that the parametrization approaches would outperform FD consistency, especially if the joint's properties are strongly frequency dependent, as the parametrization assumes frequency-independent system matrices. However, an important advantage of a parametrized joint model is the efficient consideration of resilient connections in a simulation environment. This can be achieved by establishing connections between individual numerical models using the parametrized joint models. In addition, parametrizing the joint can reduce the effects of noise due to the overdetermination with respect to frequency. Therefore, the FD approach is included in the comparison to assess how well the parametrized models are able to describe the joint dynamics compared to the less restrictive FD model.

Each graph in Fig. 12 includes the results for LS and LASSO. The LS joint models are obtained by directly solving the joint identification equations in a least-squares sense, without any regularization of the matrices being inverted. On the contrary, the LASSO joint models have an additional hyperparameter  $\lambda$  determining the penalty strength. Throughout this paper, the value of  $\lambda$  was determined by varying the parameter in conjunction with five-fold cross validation to find the value  $\lambda$  with the lowest validation error [40]. By varying the parametrization (DP or IP) and excitation direction updating (ERR or UP), four graphs are obtained. When DP is considered, there is a larger discrepancy between LS and LASSO

solutions. With IP, the LS and LASSO solutions largely overlap. When considering IP, both LS and LASSO are also significantly more consistent with the FD solution. In contrast, DP solutions are less accurate in the low-frequency range. The frequency-dependent joint model is able to accurately reproduce the assembly dynamics within the onboard validation when the updated excitation directions are considered. It can also be observed that updating excitation directions improves the parametrized joint models. The most accurate parametrized joint model was obtained by combining RBM constraints, LS, IP, and excitation direction updating.

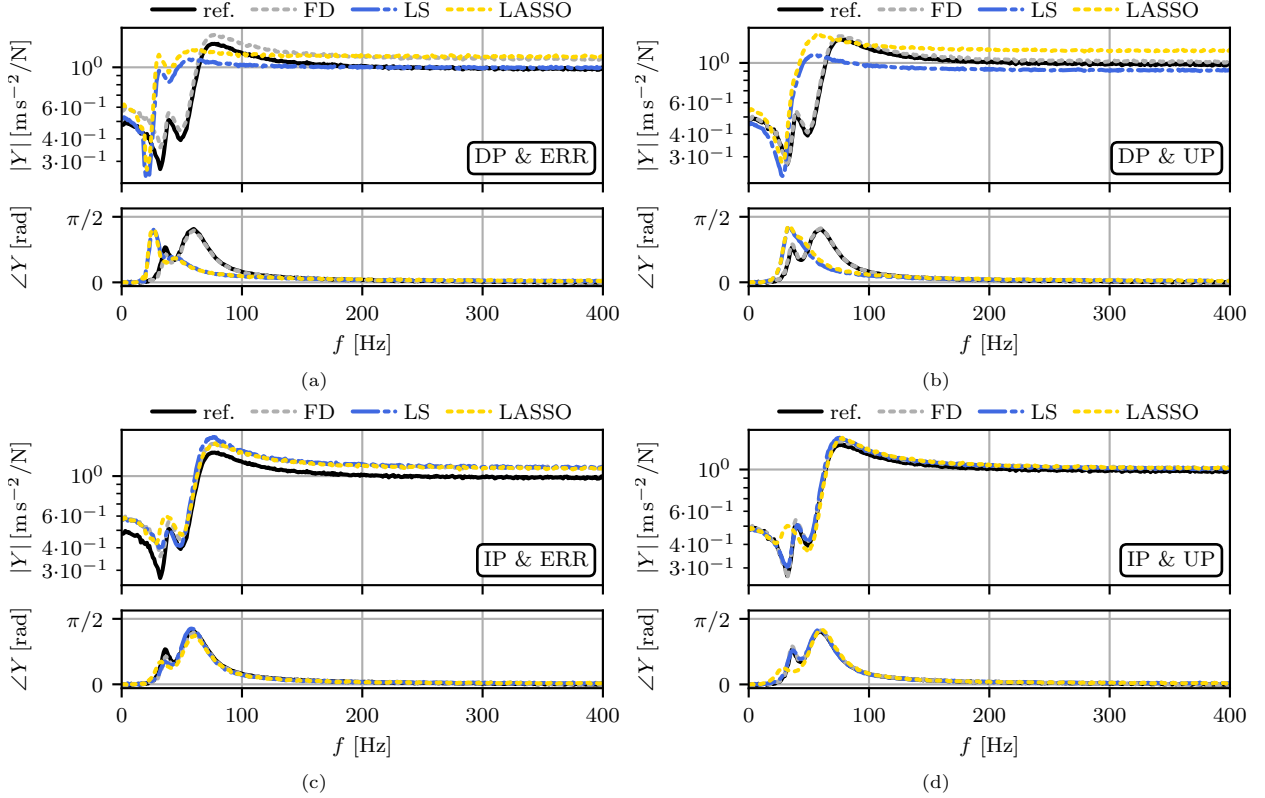


Figure 12: : Estimated CJC FRFs with RBM constraints: (a) DP without direction updating, (b) DP with direction updating, (c) IP without direction updating, (d) IP with direction updating.

The effect of LASSO is significantly more pronounced with DP compared to IP. The improvement of joint model accuracy is more pronounced with off-diagonal FRFs, i.e. FRFs corresponding to different response and excitation directions or locations, as shown in Fig. 13(a). Fig. 13(b) illustrates how LASSO affects the mass and stiffness matrices, where the nonzero elements of the matrices are represented by black tiles.

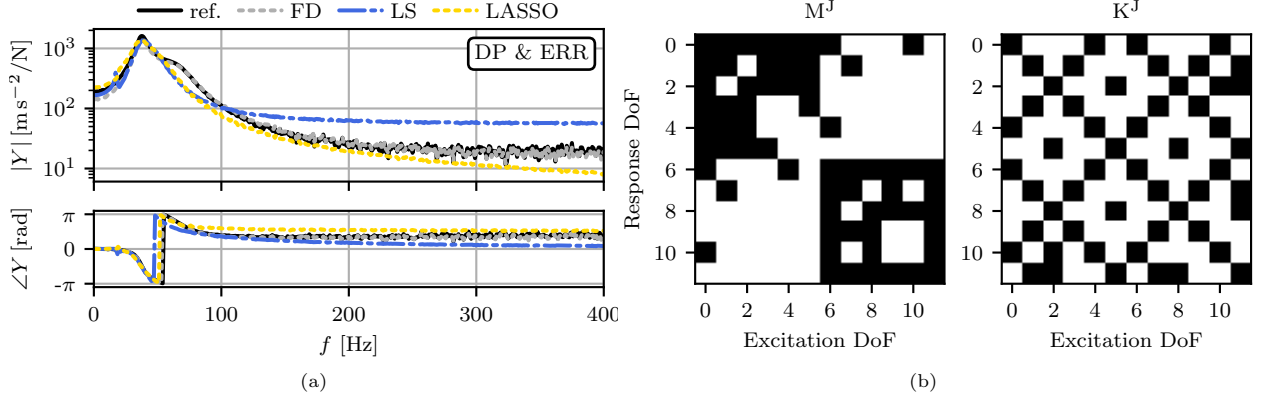


Figure 13: Joint identification with LASSO: (a) comparison of LS and LASSO on estimated off-diagonal FRFs, (b) sparsity promoting effect of LASSO on the identified mass and stiffness matrices.

The identified mass matrix is expected to be positive definite, while the damping and stiffness matrices ought to be positive semi-definite for an unsupported joint, since the damping and stiffness matrices do not oppose any rigid-body motion [43]. Inconsistencies regarding positive (semi-)definiteness are revealed by calculating the eigenvalues of the identified matrices. Positive definite matrices have strictly positive eigenvalues, while the eigenvalues of positive semi-definite matrices are non-negative. The eigenvalues of all matrices for all joint identification approaches are shown in Fig. 14. The identified mass matrices have negative eigenvalues regardless of the identification approach. None of the approaches incorporate the positive (semi-)definiteness constraint, therefore, non-positive eigenvalues arise in the mass matrices to better compensate for the discrepancy between the substructures in the uncoupled and coupled state. Both damping matrices have six zero eigenvalues under RBM constraints. RBM constraints also reduce the number of negative eigenvalues for both damping matrices. Similarly, the stiffness matrix has six zero eigenvalues under RBM constraints, with the remaining eigenvalues strictly positive. Therefore, RBM constraints provide a more physically consistent approach to joint identification without explicitly enforcing positive semi-definiteness of the damping and stiffness matrices. The remaining negative eigenvalues of the damping matrices may be present due to the FRFs being sensitive to damping only near resonance frequencies. Therefore, future studies could focus on selection of frequencies for joint identification, which may constrain the damping matrices to comply with positive semi-definiteness.

#### 4.3. Cross validation

The main utility in performing onboard validation is to validate the implementation of the identification methods. Some identification approaches may be subject to overfitting, therefore, it is recommended to assess the accuracy in a cross validation study. However, it is worth noting that the identification problem is highly overdetermined due to the parametrization, therefore, issues associated with overfitting are expected to be less severe and onboard validation can serve as an initial assessment tool.

Cross validation is performed by coupling the individual joint models with substructures A and B to estimate the AJB FRFs, where A and B are connected by two joints (Fig. 6). Cross validation results are shown in Fig. 15. It was again observed that RBM constraints improve the accuracy at low frequencies without affecting the higher-frequency range, while neglecting RBMs resulted in a similar deviation at low frequencies, as observed in the onboard validation. Therefore, all results presented in Fig. 15 take RBM constraints into consideration. Consistent with the onboard validation, the effect of LASSO is more pronounced with DP, while IP yields similar results for both LS and LASSO. Furthermore, updating excitation directions noticeably improves the identification accuracy, which can be more clearly observed compared to the onboard validation.<sup>6</sup> Again, the highest accuracy is achieved by considering RBM constraints, updated

<sup>6</sup>Onboard validation is less sensitive to measurement errors, as the decoupled and subsequently coupled substructure models

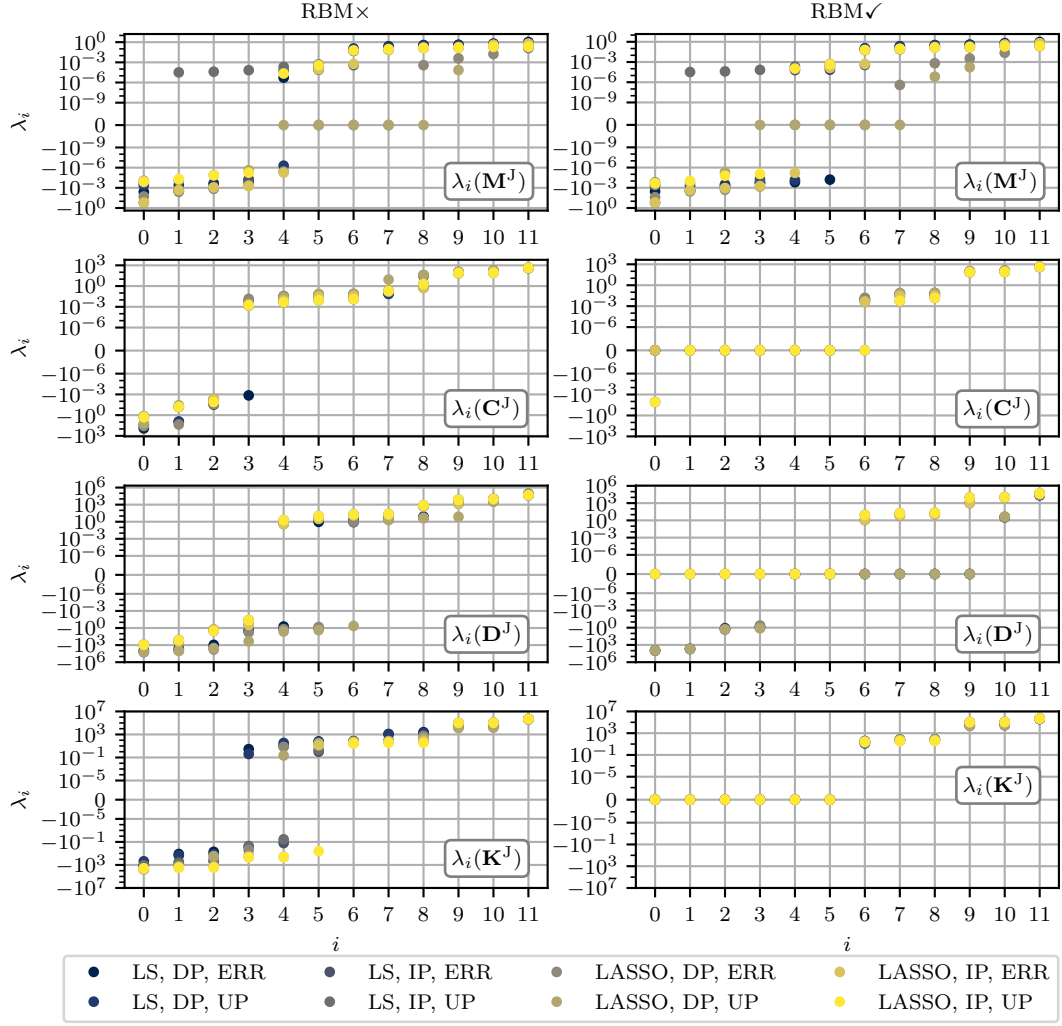


Figure 14: Effect of RBM constraints on eigenvalues of the joint's system matrices in the numerical study.

excitation directions, and IP, with no significant differences between the LS and LASSO solutions. Comparing the parametrized joint models to the FD model, the noise-filtering property of the parametrization approaches can be observed. Due to the overdetermination with respect to frequency, the effects of noise are significantly reduced.

are exactly the same. Although an erroneous joint model may be obtained in the identification process, the effect of these errors are diminished by coupling the same erroneous substructure models. In contrast, cross validation is performed by coupling different substructure models, therefore, the errors compound and are more pronounced in the validation step.

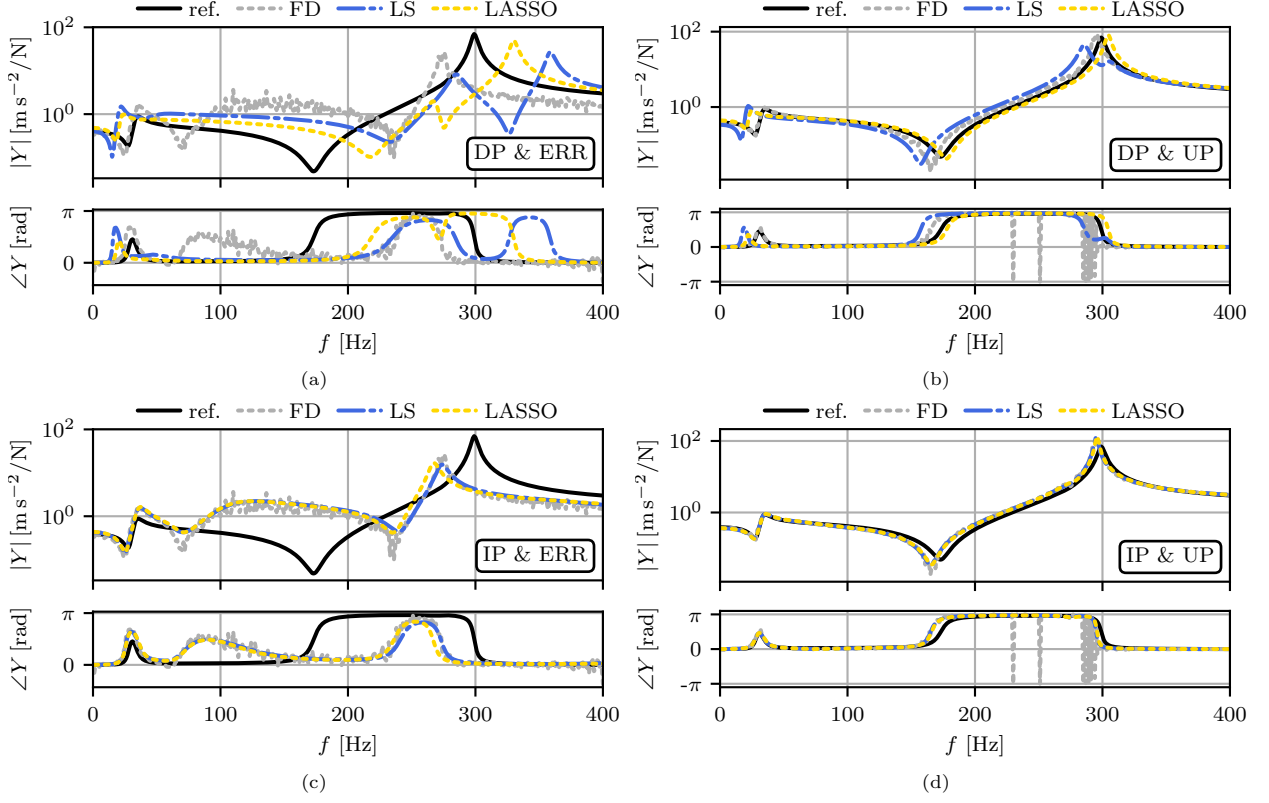


Figure 15: Estimated AJB FRFs with RBM constraints: (a) DP without direction updating, (b) DP with direction updating, (c) IP without direction updating, (d) IP with direction updating.

In line with the onboard validation, the improvement of the LASSO solution compared to LS can be most notably observed on the estimated off-diagonal FRFs with DP. A comparison of LS and LASSO solutions for both DP and IP is shown in Fig. 16. Compared to LS, LASSO is able to achieve a higher accuracy with DP, while the difference between LS and LASSO is negligible with IP.

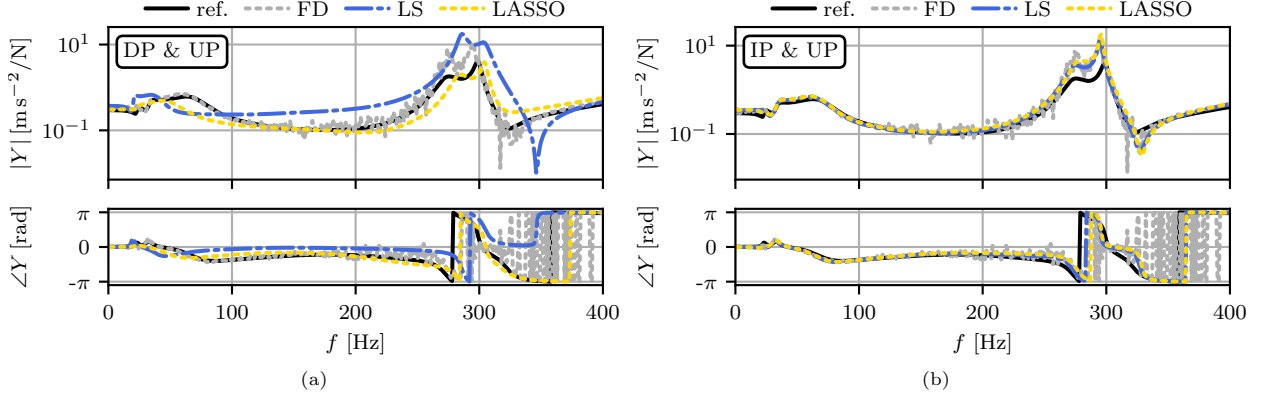


Figure 16: Comparison of LS and LASSO on estimated off-diagonal FRFs with updated excitation directions: (a) DP, (b) IP.

To further validate the proposed modifications to the joint identification procedure, an alternative assembly depicted in Fig. 17, denoted as  $\overline{\text{AJB}}$ , was considered for the joint identification, consisting of the A and B substructures connected by a single joint. First, the  $\overline{\text{AJB}}$  structure was used to isolate the joint using the proposed parametrization approaches. An additional cross validation was performed by coupling the A and B substructures with the identified joint at the two connection points of each substructure. This allows to verify the proposed approaches are independent of the substructures connected by the joint in the identification stage. Since excitation direction updating does not directly alter the identification procedure, only true excitation directions were considered in the alternative joint identification. The effects of RBM constraints, LASSO, and IP on the additional cross validation are shown in Fig. 18. Similar to the previous cross validation, LASSO significantly improves results when applied to DP, while IP yields similar results for both LS and LASSO. In all cases, RBM constraints improve the consistency of the estimated assembly dynamics at low frequencies.

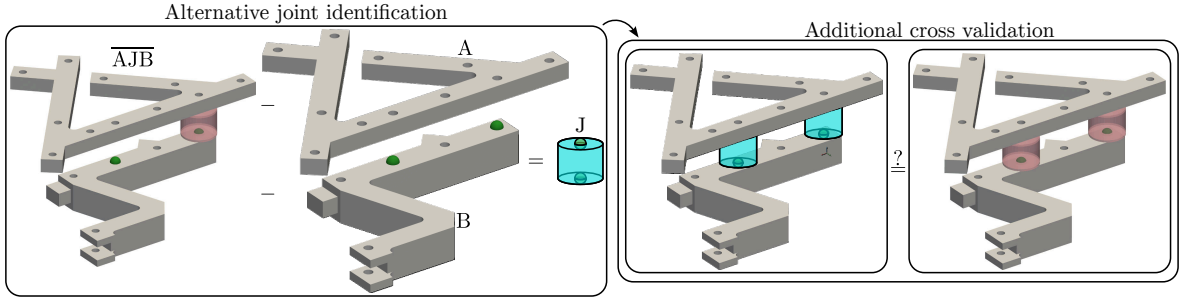


Figure 17: Joint identification on the alternative  $\overline{\text{AJB}}$  assembly and subsequent cross validation.

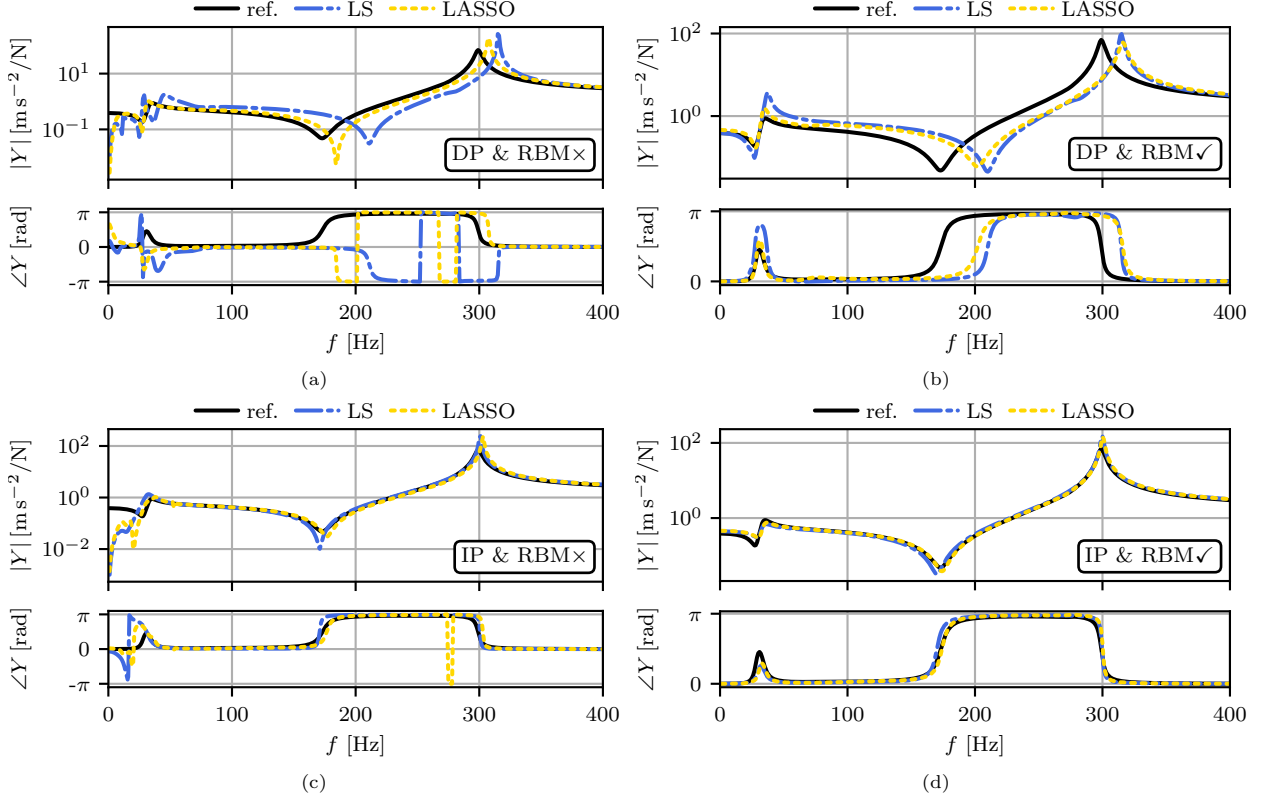


Figure 18: : Estimated AJB FRFs based on the joint identified from the  $\overline{\text{AJB}}$  assembly: (a) DP without RBM constraints, (b) DP with RBM constraints, (c) IP without RBM constraints, (d) IP with RBM constraints.

## 5. Experimental study

The numerical study was designed to resemble the upcoming experimental study to capture any substructuring or identification related issues. The substructures in the experimental study were of similar geometry. Substructures involved in the joint identification procedure are shown in Fig. 19. Both upper and lower cross substructures were equipped with four triaxial accelerometers, and twelve excitation locations were distributed on each cross. The measured substructures were suspended by elastic bungee cords to approximate free boundary conditions.

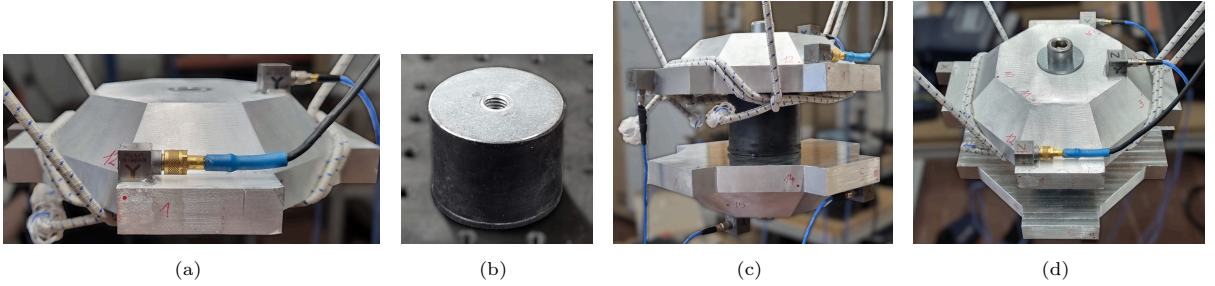


Figure 19: Identification and onboard validation substructures within experimental joint identification: (a) C, (b) J, (c) CJC (side view), (d) CJC (top view).

Substructures involved in the experimental cross validation are shown in Fig. 20. In the assembled configuration, the substructures A and B are physically connected by two joints. Threaded plates on both

sides of the rubber mounts allowed to connect the individual substructures using bolts. The interface of each substructure is modeled using two six-DoF virtual points. To facilitate excitation of the substructures in different directions, auxiliary blocks were mounted to the substructures. Three triaxial accelerometers and three auxiliary blocks were mounted in the proximity of each VP. Three impacts were located on each auxiliary block for a total of nine impacts per VP. These substructures were also suspended by bungee cords to approximate free boundary conditions. Three additional excitation locations and a triaxial accelerometer were placed away from the interface on each substructure to compare the true and estimated FRFs.

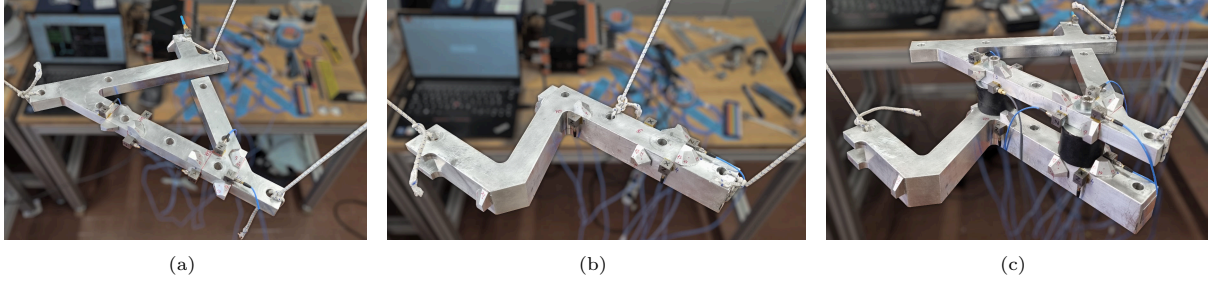


Figure 20: Cross validation substructures within experimental joint identification: (a) A, (b) B, (c) AJB.

### 5.1. Validation of the joint model

Due to the absence of direct joint impedance measurements, the impedances obtained by different parametrization approaches can be compared to the FD impedance. Fig. 21 compares the driving-point impedances of the  $u_{1z}$  DoF with respect to Fig. 1. For brevity, the impedances are shown only for RBM constraints and updated excitation directions. As observed in the numerical study, the discrepancy between LS and LASSO is larger with DP and negligible with IP. Parametrization of the joint model further reduces the effect of noise compared to the FD approach. Comparing DP and IP regarding joint impedance, IP aligns more closely with FD.

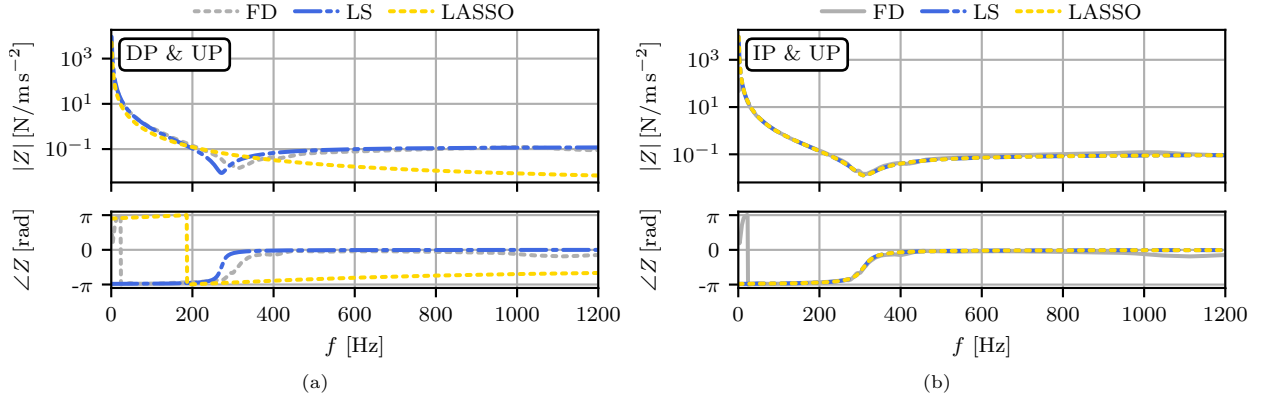


Figure 21: Joint impedance obtained by considering RBM constraints and updated excitation directions: (a) DP, (b) IP.

In line with the numerical study, the eigenvalues of the joint's system matrices were also calculated in the experimental study, as shown in Fig. 22. Again, negative eigenvalues are present in the mass matrix regardless of the approach. Under RBM constraints, damping matrices exhibit significantly fewer negative eigenvalues and six zero eigenvalues. Stiffness matrices are again strictly positive semi-definite under RBM constraints.

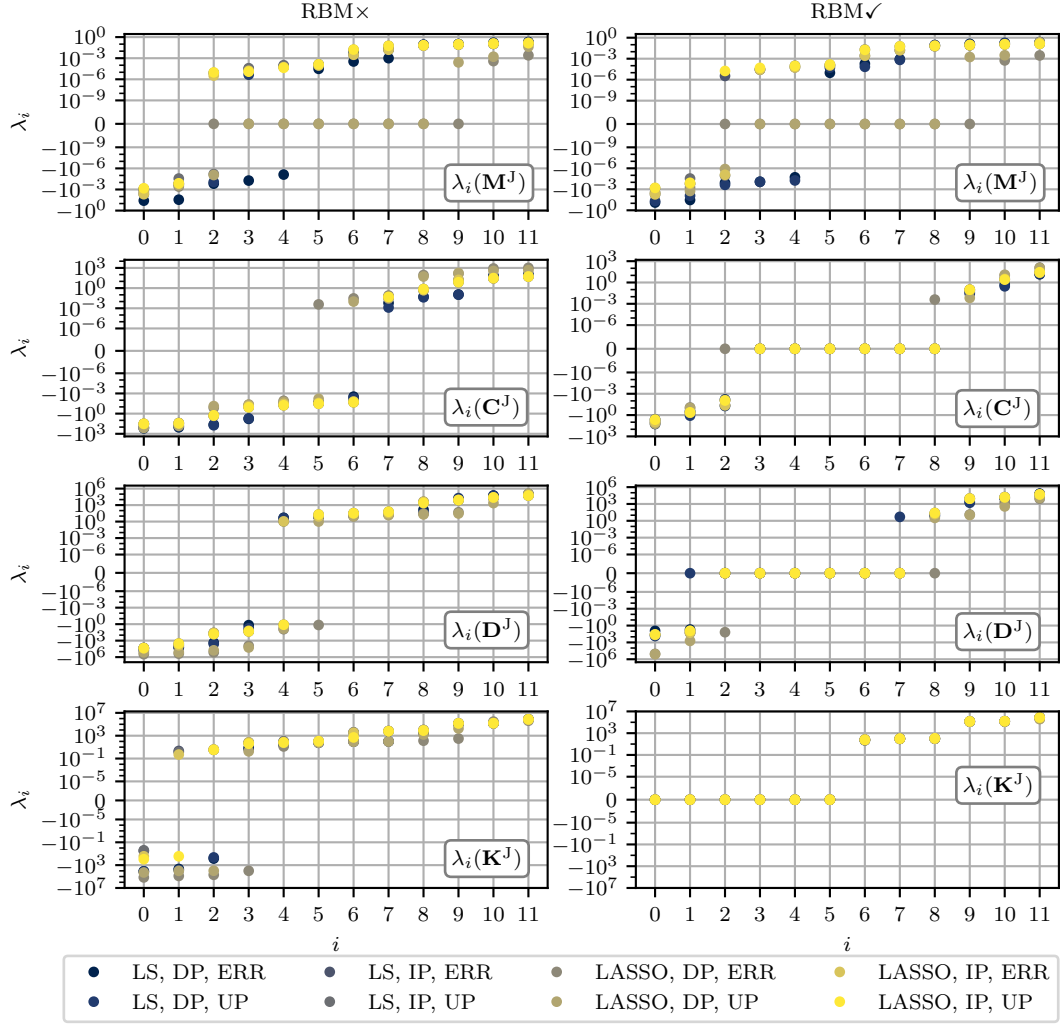


Figure 22: Effect of RBM constraints on eigenvalues of the joint's system matrices in the experimental study.

## 5.2. Cross validation

For the sake of brevity, only cross validation results are presented in the experimental study, although similar conclusions could be drawn from onboard validation. Cross validation results, where the FRFs of the AJB assembly are estimated, are shown in Fig. 23. Only the models which consider RBM constraints are compared, as the accuracy at low frequencies was improved without affecting the higher-frequency range. Compared to DP, the results obtained by IP align better with the FD model. Furthermore, updating excitation directions consistently improved the model accuracy, regardless of the specific approach. Overall, the highest accuracy was achieved by combining RBM constraints, LS, IP, and excitation direction updating. As is the case with the numerical study, LASSO was able to achieve the highest accuracy improvement in the case of DP and non-updated excitation directions. Similar conclusions can be drawn from Fig. 24, where the coherence (Eq. (82)) of FRFs in Fig. 23 with respect to the measured (reference) FRF is shown in a form of a bar chart.

Promoting a sparse solution within the joint identification procedure leads to an improved accuracy of DP with non-updated excitation directions. Future studies focusing on applying sparse regression methods may be able to further improve the overall accuracy for all models, or at least for the IP approach. The ability of LASSO to improve the accuracy of DP & ERR model may be attributed to neglecting a significant

number of the off-diagonal terms in the joint's mass and stiffness matrices. These terms are nonzero when performing LS, however, their values may compensate for the errors in the excitation directions. As these errors are diminished by updating excitation directions, neglecting the off-diagonal terms of the mass and stiffness matrices does not reflect an improvement in joint accuracy.

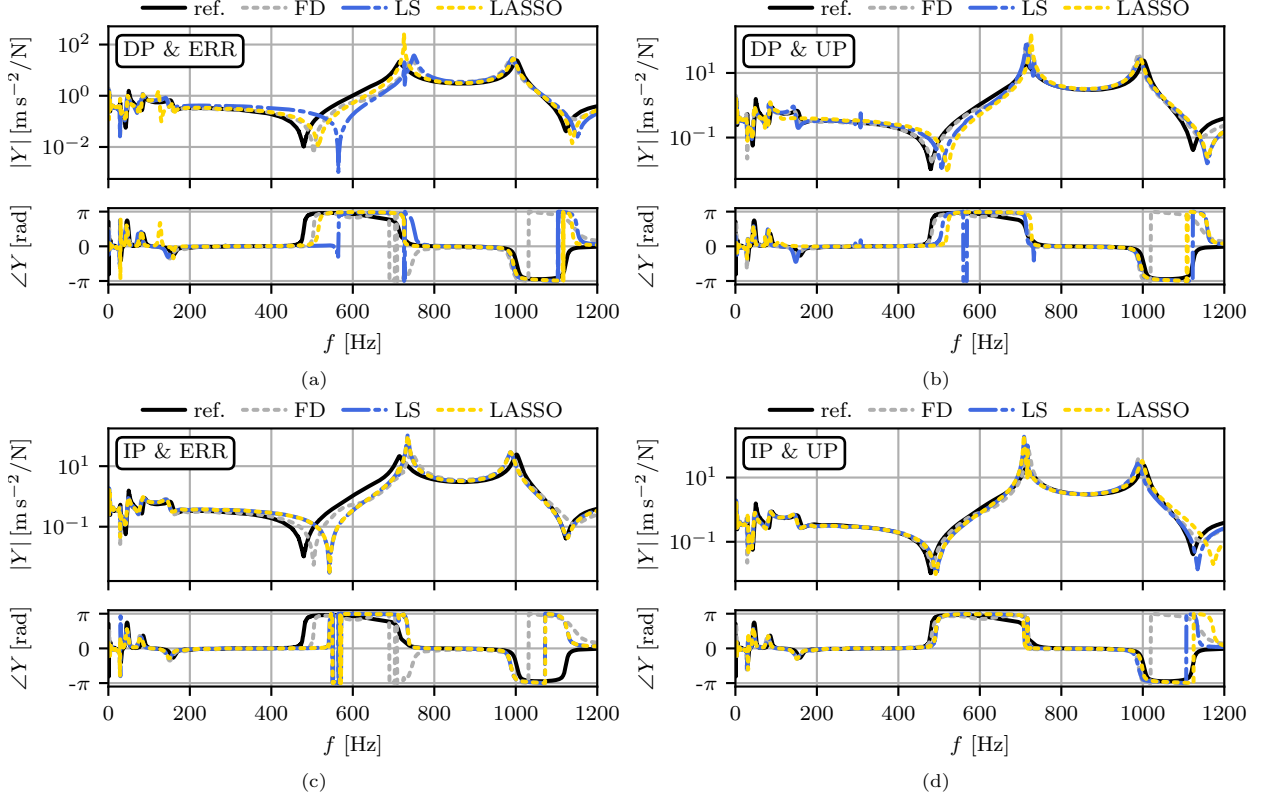


Figure 23: Estimated AJB FRFs with RBM constraints: (a) DP without direction updating, (b) DP with direction updating, (c) IP without direction updating, (d) IP with direction updating.

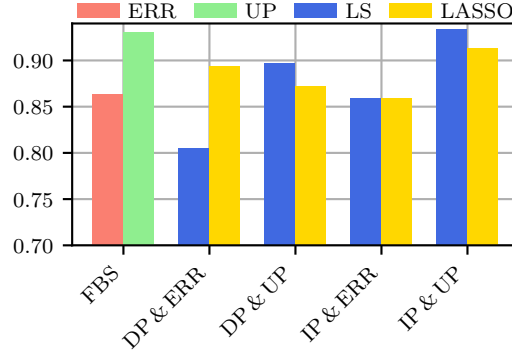


Figure 24: Average coherence of the estimated AJB FRFs with respect to the measured (reference) AJB FRFs.

## 6. Conclusions

Performing joint identification in the form of model parametrization is often required for the purposes of subsequent numerical simulations, therefore, obtaining a valid joint model is essential. A reformulation of the joint identification approach described in [8] is presented, inspired by the LM-FBS derivation, along with four modifications to the identification approach:

1. IP - indirect parametrization modifies the existing parametrization procedure by first obtaining the joint's dynamic stiffness matrix, followed by the parametrization.
2. RBM constraints – the twelve-DoF joint model considers free boundary conditions, therefore, the damping and stiffness matrices should require no force for rigid-body motion.
3. LASSO - promoting sparsity in the joint's system matrices may remove terms sensitive to measurement errors.
4. Excitation direction updating - when modeling the interface using the VPT, the errors in excitation directions can significantly decrease the VPT accuracy. Updating the excitation directions may therefore improve the joint identification accuracy.

All of the above approaches were tested with the aim of improving the joint model accuracy. Their application is mutually independent, therefore, 16 distinct identification approaches were considered by accounting for all possible combinations. Considering the joint RBMs for obtaining the stiffness and damping matrices improved the joint model accuracy at low frequencies regardless of the specific approach. In addition, the stiffness matrices become strictly positive semi-definite under RBM constraints, while the number of negative eigenvalues is reduced for both damping matrices. Performing excitation direction updating improved the accuracy of the identified joint in both the numerical and experimental studies. Similarly, IP reflected in increased joint model accuracy. The highest accuracy was achieved by combining RBM constraints and IP with excitation direction updating, where LS outperformed LASSO. The parametrization approaches were also compared to the less restrictive frequency-dependent joint identification to assess their capacity to describe the joint dynamics. The parametrized models were consistent with the FD model, while reducing the effect of noise.

It is worth noting that LASSO was able to outperform LS when combining DP with non-updated excitation directions. Increased accuracy due to neglected terms within the joint's mass and stiffness matrices may be attributed to the erroneous excitation directions. By updating excitation directions, the main source of error is accounted for, leading to LASSO no longer reflecting an increase in joint model accuracy. Future work may further investigate the application of LASSO or alternative sparse regression approaches with the aim of improving joint model's accuracy by neglecting the terms sensitive to experimental errors.

Additional improvements may be achieved by forming a criterion for the selection of frequencies considered for the joint parametrization, similar to [14]. Since FRFs are most sensitive to the damping parameters only near the resonance frequencies, LASSO promotes the sparsity of damping matrices to the point of

their removal when a broad frequency range is considered. Therefore, LASSO was applied to promote sparsity only for mass and stiffness matrices. Additional attention concerning the selected frequencies for the parametrization may allow for a sparsity promoting approach to identify the damping matrices without their complete removal.

### CRedit authorship contribution statement

**Jure Korbar:** Conceptualization, Methodology, Software, Investigation, Formal analysis, Validation, Writing – original draft, Writing – review & editing, Visualization. **Domen Očeppek:** Conceptualization, Methodology, Investigation, Formal analysis, Writing – review & editing. **Miha Pogačar:** Validation, Writing – review & editing. **Gregor Čepon:** Writing – review & editing, Project administration, Resources, Supervision.

### Declaration of competing interests

The authors declare that they have no known competing financial interests or personal relationships that could have appeared to influence the work reported in this paper.

### Acknowledgments

The authors acknowledge partial financial support from the European Union’s Horizon Europe research and innovation program under grant agreement No. 101091536 (DICIM project) and grant agreement No. 101138182 (CREDIT project) and also the partial financial support from the Slovenian Research Agency (research project L2-60145 and research core funding No. P2-0263).

### Appendix A. Applying LASSO to a subset of variables

The problem of applying LASSO regression to only a subset of all variables is formulated as:

$$\hat{\mathbf{p}}_{\text{mk}}, \hat{\mathbf{p}}_{\text{cd}} = \underset{\mathbf{p}_{\text{mk}}, \mathbf{p}_{\text{cd}}}{\operatorname{argmin}} \left( \|\mathbf{y} - \mathbf{A}_{\text{mk}}\mathbf{p}_{\text{mk}} - \mathbf{A}_{\text{cd}}\mathbf{p}_{\text{cd}}\|_2^2 + \lambda \|\mathbf{p}_{\text{mk}}\|_1 \right), \quad (\text{A.1})$$

where the penalized variables are denoted as  $\mathbf{p}_{\text{mk}}$  and the non-penalized variables are  $\mathbf{p}_{\text{cd}}$ . By expanding the squared 2-norm in Eq. (A.1) and writing the right-hand side as a function  $f(\mathbf{p}_{\text{mk}}, \mathbf{p}_{\text{cd}})$  to be minimized, the following is obtained:

$$\begin{aligned} f(\mathbf{p}_{\text{mk}}, \mathbf{p}_{\text{cd}}) &= (\mathbf{y} - \mathbf{A}_{\text{mk}}\mathbf{p}_{\text{mk}} - \mathbf{A}_{\text{cd}}\mathbf{p}_{\text{cd}})^\top (\mathbf{y} - \mathbf{A}_{\text{mk}}\mathbf{p}_{\text{mk}} - \mathbf{A}_{\text{cd}}\mathbf{p}_{\text{cd}}) + \lambda \|\mathbf{p}_{\text{mk}}\|_1, \\ &= \mathbf{y}^\top \mathbf{y} + \mathbf{p}_{\text{mk}}^\top \mathbf{A}_{\text{mk}}^\top \mathbf{A}_{\text{mk}} \mathbf{p}_{\text{mk}} + \mathbf{p}_{\text{cd}}^\top \mathbf{A}_{\text{cd}}^\top \mathbf{A}_{\text{cd}} \mathbf{p}_{\text{cd}} \\ &\quad - 2\mathbf{p}_{\text{mk}}^\top \mathbf{A}_{\text{mk}}^\top \mathbf{y} - 2\mathbf{p}_{\text{cd}}^\top \mathbf{A}_{\text{cd}}^\top \mathbf{y} + 2\mathbf{p}_{\text{cd}}^\top \mathbf{A}_{\text{cd}}^\top \mathbf{A}_{\text{mk}} \mathbf{p}_{\text{mk}}. \end{aligned} \quad (\text{A.2})$$

The minimum of  $f$  can be found at  $\mathbf{p}_{\text{cd}} = \hat{\mathbf{p}}_{\text{cd}}$  and  $\mathbf{p}_{\text{mk}} = \hat{\mathbf{p}}_{\text{mk}}$ . The value of  $\hat{\mathbf{p}}_{\text{cd}}$  can be expressed with  $\mathbf{p}_{\text{mk}}$  by setting the gradient of  $f$  with respect to  $\mathbf{p}_{\text{cd}}$  to zero:

$$\begin{aligned} \nabla_{\mathbf{p}_{\text{cd}}} f(\mathbf{p}_{\text{mk}}, \hat{\mathbf{p}}_{\text{cd}}) &= \mathbf{0}, \\ 2\mathbf{A}_{\text{cd}}^\top \mathbf{A}_{\text{cd}} \hat{\mathbf{p}}_{\text{cd}} - 2\mathbf{A}_{\text{cd}}^\top \mathbf{y} + 2\mathbf{A}_{\text{cd}}^\top \mathbf{A}_{\text{mk}} \mathbf{p}_{\text{mk}} &= \mathbf{0}, \\ \mathbf{A}_{\text{cd}}^\top \mathbf{A}_{\text{cd}} \hat{\mathbf{p}}_{\text{cd}} &= \mathbf{A}_{\text{cd}}^\top \mathbf{y} - \mathbf{A}_{\text{cd}}^\top \mathbf{A}_{\text{mk}} \mathbf{p}_{\text{mk}}, \\ \hat{\mathbf{p}}_{\text{cd}} &= (\mathbf{A}_{\text{cd}}^\top \mathbf{A}_{\text{cd}})^{-1} \mathbf{A}_{\text{cd}}^\top \mathbf{y} - (\mathbf{A}_{\text{cd}}^\top \mathbf{A}_{\text{cd}})^{-1} \mathbf{A}_{\text{cd}}^\top \mathbf{A}_{\text{mk}} \mathbf{p}_{\text{mk}}. \end{aligned} \quad (\text{A.3})$$

Replacing  $\mathbf{p}_{\text{cd}}$  in Eq. (A.2) with  $\hat{\mathbf{p}}_{\text{cd}}$  from Eq. (A.3) eliminates the dependency of  $f$  on  $\mathbf{p}_{\text{cd}}$  by implicitly accounting for the zero-gradient requirement with respect to  $\mathbf{p}_{\text{cd}}$ :

$$f(\mathbf{p}_{\text{mk}}) = \left\| \mathbf{y} - \mathbf{A}_{\text{mk}}\mathbf{p}_{\text{mk}} - \mathbf{A}_{\text{cd}} \left( (\mathbf{A}_{\text{cd}}^\top \mathbf{A}_{\text{cd}})^{-1} \mathbf{A}_{\text{cd}}^\top \mathbf{y} - (\mathbf{A}_{\text{cd}}^\top \mathbf{A}_{\text{cd}})^{-1} \mathbf{A}_{\text{cd}}^\top \mathbf{A}_{\text{mk}} \mathbf{p}_{\text{mk}} \right) \right\|_2^2 + \lambda \|\mathbf{p}_{\text{mk}}\|_1. \quad (\text{A.4})$$

For brevity, the projection matrix of  $\mathbf{A}_{cd}$  is defined as:

$$\mathbf{H}_{cd} = \mathbf{A}_{cd} (\mathbf{A}_{cd}^\top \mathbf{A}_{cd})^{-1} \mathbf{A}_{cd}^\top. \quad (\text{A.5})$$

Distributing the product in Eq. (A.4) and considering Eq. (A.5) yields:

$$f(\mathbf{p}_{mk}) = \|(\mathbf{I} - \mathbf{H}_{cd}) \mathbf{y} - (\mathbf{I} - \mathbf{H}_{cd}) \mathbf{A}_{mk} \mathbf{p}_{mk}\|_2^2 + \lambda \|\mathbf{p}_{mk}\|_1. \quad (\text{A.6})$$

Defining  $\tilde{\mathbf{y}} \triangleq (\mathbf{I} - \mathbf{H}_{cd}) \mathbf{y}$  and  $\tilde{\mathbf{A}}_{mk} \triangleq (\mathbf{I} - \mathbf{H}_{cd}) \mathbf{A}_{mk}$ , the problem in Eq. (A.1) is reformulated to an ordinary LASSO problem:

$$\hat{\mathbf{p}}_{mk} = \underset{\mathbf{p}_{mk}}{\operatorname{argmin}} (f(\mathbf{p}_{mk})) = \underset{\mathbf{p}_{mk}}{\operatorname{argmin}} \left( \|\tilde{\mathbf{y}} - \tilde{\mathbf{A}}_{mk} \mathbf{p}_{mk}\|_2^2 + \lambda \|\mathbf{p}_{mk}\|_1 \right). \quad (\text{A.7})$$

## References

- [1] D. De Klerk, D. J. Rixen, S. N. Voormeeren, General framework for dynamic substructuring: history, review and classification of techniques, *AIAA Journal* 46 (5) (2008) 1169–1181. doi:10.2514/1.33274.
- [2] R. L. Mayes, Tutorial on experimental dynamic substructuring using the transmission simulator method, 2012, pp. 1–9. doi:10.1007/978-1-4614-2422-2\_1.
- [3] J.-S. Tsai, Y.-F. Chou, The identification of dynamic characteristics of a single bolt joint, *Journal of Sound and Vibration* 125 (3) (1988) 487–502. doi:10.1016/0022-460X(88)90256-8.
- [4] M. Kreutz, F. Trainotti, V. Gimpl, D. J. Rixen, On the robust experimental multi-degree-of-freedom identification of bolted joints using frequency-based substructuring, *Mechanical Systems and Signal Processing* 203 (2023). doi:10.1016/j.ymssp.2023.110626.
- [5] L. Gagliardini, D. de Klerk, Stiffness injection: A tool for vehicle NVH performance optimization, in: 12th International Styrian Noise, Vibration & Harshness Congress: The European Automotive Noise Conference, 2022. doi:10.4271/2022-01-0976.
- [6] M. Haeussler, S. W. B. Klaassen, D. J. Rixen, Experimental twelve degree of freedom rubber isolator models for use in substructuring assemblies, *Journal of Sound and Vibration* 474 (2020). doi:10.1016/j.jsv.2020.115253.
- [7] J. Wang, C. Liou, Identification of parameters of structural joints by use of noise-contaminated FRFs, *Journal of Sound and Vibration* 142 (2) (1990) 261–277. doi:10.1016/0022-460X(90)90556-F.
- [8] Y. Ren, C. F. Beards, Identification of joint properties of a structure using FRF data, *Journal of Sound and Vibration* 186 (4) (1995) 567–587. doi:10.1006/jsvi.1995.0469.
- [9] Y. Ren, C. Beards, Identification of ‘effective’ linear joints using coupling and joint identification techniques (1998). doi:10.1115/1.2893835.
- [10] T. Yang, S.-H. Fan, C.-S. Lin, Joint stiffness identification using FRF measurements, *Computers & Structures* 81 (28–29) (2003) 2549–2556. doi:10.1016/S0045-7949(03)00328-6.
- [11] D. Čelič, M. Boltežar, Identification of the dynamic properties of joints using frequency–response functions, *Journal of Sound and Vibration* 317 (1–2) (2008) 158–174. doi:10.1016/j.jsv.2008.03.009.
- [12] D. Čelič, M. Boltežar, The influence of the coordinate reduction on the identification of the joint dynamic properties, *Mechanical Systems and Signal Processing* 23 (4) (2009) 1260–1271. doi:10.1016/j.ymssp.2008.11.002.
- [13] M. Wang, D. Wang, G. Zheng, Joint dynamic properties identification with partially measured frequency response function, *Mechanical Systems and Signal Processing* 27 (2012) 499–512. doi:10.1016/j.ymssp.2011.09.024.
- [14] F. Batista, N. Maia, An iterative uncoupling technique for the identification of the dynamic properties of joints (2012).
- [15] M. Mehrpouya, E. Graham, S. S. Park, FRF based joint dynamics modeling and identification, *Mechanical Systems and Signal Processing* 39 (1–2) (2013) 265–279. doi:10.1016/j.ymssp.2013.03.022.
- [16] M. Mehrpouya, E. Graham, S. S. Park, Identification of multiple joint dynamics using the inverse receptance coupling method, *Journal of Vibration and Control* 21 (16) (2014) 3431–3449. doi:10.1177/1077546314523306.
- [17] M. Mehrpouya, M. Sanati, S. S. Park, Identification of joint dynamics in 3D structures through the inverse receptance coupling method, *International Journal of Mechanical Sciences* 105 (2016) 135–145. doi:10.1016/j.ijmecsci.2015.11.007.
- [18] J. W. R. Meggitt, A. T. Moorhouse, In-situ sub-structure decoupling of resiliently coupled assemblies, *Mechanical Systems and Signal Processing* 117 (2019) 723–737. doi:10.1016/j.ymssp.2018.07.045.
- [19] M. van der Seijs, D. van den Bosch, D. J. Rixen, D. de Klerk, An improved methodology for the virtual point transformation of measured frequency response functions in dynamic substructuring, *COMPDYN* (2013). doi:10.7712/120113.4816.C1539.
- [20] S. W. B. Klaassen, M. van der Seijs, D. de Klerk, System equivalent model mixing, *Mechanical Systems and Signal Processing* 105 (2018) 90–112. doi:10.1016/j.ymssp.2017.12.003.
- [21] S. W. B. Klaassen, D. J. Rixen, Using SEMM to identify the joint dynamics in multiple degrees of freedom without measuring interfaces, 2020, pp. 87–99. doi:10.1007/978-3-030-12184-6\_10.
- [22] Z. Saeed, S. W. Klaassen, C. M. F. F. Berruti, D. J. Rixen, M. Brake, Joint Identification in Bladed-disks using SEMM and VPT, *Tribomechadynamics*, 2019.

- [23] Z. Saeed, S. W. Klaassen, C. M. Firrone, T. M. Berruti, D. J. Rixen, Experimental joint identification using system equivalent model mixing in a bladed disk, *Journal of Vibration and Acoustics* 142 (5) (2020). doi:10.1115/1.4047361.
- [24] Z. Saeed, M. Kazeminasab, C. M. Firrone, T. M. Berruti, et al., Improved identification of a blade-disk coupling through a parametric study of the dynamic hybrid models, in: *ISMA 2020-International Conference on Noise and Vibration Engineering*, 2020, pp. 1323–1336.
- [25] Z. Saeed, C. M. Firrone, T. M. Berruti, Joint identification through hybrid models improved by correlations, *Journal of Sound and Vibration* 494 (2021). doi:10.1016/j.jsv.2020.115889.
- [26] M. Di Manno, J. Brunetti, W. D'Ambrogio, A. Fregolent, A critical evaluation of SEMM-based joint identification procedure to reduce the error propagation effects, *Mechanical Systems and Signal Processing* 208 (2024). doi:10.1016/j.ymssp.2023.111063.
- [27] Z. Saeed, C. Firrone, T. Berruti, Substructuring for contact parameters identification in bladed-disks, Vol. vol. 1264, no. 1 of *Journal of Physics: Conference Series*, 2019. doi:10.1088/1742-6596/1264/1/012037.
- [28] D. Ocepek, F. Trainotti, G. Čepón, D. J. Rixen, M. Boltežar, On the experimental coupling with continuous interfaces using frequency based substructuring, *Mechanical Systems and Signal Processing* 217 (2024). doi:10.1016/j.ymssp.2024.111517.
- [29] D. Minervini, A. Stella, Experimental frequency-based decoupling for tire characterization, in: *Proceedings of ISMA2022 International Conference on Noise and Vibration Engineering*, 2022.
- [30] S. Zhang, H. Devriendt, L. Van Belle, W. Desmet, Substructuring-based parametric reduced-order modelling for structural dynamic predictions of bolted assemblies, *Mechanical Systems and Signal Processing* 218 (2024). doi:https://doi.org/10.1016/j.ymssp.2024.111513.
- [31] M. Brøns, F. Trainotti, D. J. Rixen, A novel optimization framework using frequency-based substructuring for estimation of linear bolted joint stiffness and damping, *Mechanical Systems and Signal Processing* 223 (2025). doi:10.1016/j.ymssp.2024.111806.
- [32] M. Brøns, F. Trainotti, D. J. Rixen, Estimating Linear Joint Stiffness and Damping Using a Frequency-Based Optimization Framework and the Emerging Concept of DyDis, 2025, pp. 37–42. doi:10.1007/978-3-031-68897-3\_4.
- [33] S. Zhang, H. Devriendt, L. Van Belle, W. Desmet, Substructuring based parametric reduced order modelling for large-scale dynamical systems containing viscoelasticity with application to bonded assemblies, *Mechanical Systems and Signal Processing* 191 (2023). doi:10.1016/j.ymssp.2023.110192.
- [34] K. Shrivastava, K. Vijayan, S. Gupta, A. Mahato, S. Roy, V. Arora, Welded joints stiffness and damping characterisation based on model updating and texture analysis, *Mechanical Systems and Signal Processing* 220 (2024). doi:10.1016/j.ymssp.2024.111684.
- [35] A. Zucchini, A. Hülsmann, F. Naets, A methodology for the experimental characterization of rubber isolators with frequency and preload dependency, *Mechanical Systems and Signal Processing* 225 (2025). doi:10.1016/j.ymssp.2024.112225.
- [36] J. Korbar, D. Ocepek, G. Čepón, M. Boltežar, Training artificial neural networks using substructuring techniques: Application to joint identification, *Mechanical Systems and Signal Processing* 198 (2023). doi:10.1016/j.ymssp.2023.110426.
- [37] T. Vrtač, D. Ocepek, M. Česnik, G. Čepón, M. Boltežar, A hybrid modeling strategy for training data generation in machine learning-based structural health monitoring, *Mechanical Systems and Signal Processing* 207 (2024). doi:10.1016/j.ymssp.2023.110937.
- [38] J. Meggitt, A. Moorhouse, A covariance based framework for the propagation of correlated uncertainty in frequency based dynamic sub-structuring, *Mechanical Systems and Signal Processing* 136 (2020). doi:10.1016/j.ymssp.2019.106505.
- [39] F. Trainotti, M. Haeussler, D. Rixen, A practical handling of measurement uncertainties in frequency based substructuring, *Mechanical Systems and Signal Processing* 144 (2020). doi:10.1016/j.ymssp.2020.106846.
- [40] R. Tibshirani, Regression Shrinkage and Selection via the Lasso, *Journal of the Royal Statistical Society: Series B (Methodological)* 58 (1) (1996) 267–288. doi:10.1111/j.2517-6161.1996.tb02080.x.
- [41] G. Čepón, D. Ocepek, J. Korbar, T. Bregar, M. Boltežar, Sensitivity-based characterization of the bias errors in frequency based substructuring, *Mechanical Systems and Signal Processing* 170 (2022). doi:10.1016/j.ymssp.2021.108800.
- [42] J. R. Magnus, H. Neudecker, The elimination matrix: some lemmas and applications, *SIAM Journal on Algebraic Discrete Methods* 1 (4) (1980) 422–449. doi:10.1137/0601049.
- [43] A. M. Kabe, B. H. Sako, Chapter 6 - Multi-degree-of-freedom systems, Vol. vol. I of *Structural Dynamics Fundamentals and Advanced Applications*, 2020, pp. 333–435. doi:10.1016/B978-0-12-821614-9.00006-9.
- [44] D. Ocepek, F. Trainotti, J. Korbar, D. J. Rixen, M. Boltežar, G. Čepón, Exploring and applying sparse regression in admittance-based TPA methods, in: *Proceedings of ISMA2024 International Conference on Noise and Vibration Engineering*, 2024.
- [45] D. J. Rixen, How measurement inaccuracies induce spurious peaks in frequency based substructuring, 2008.
- [46] E. A. Pasma, M. van der Seijs, S. W. B. Klaassen, M. W. van der Kooij, Frequency based substructuring with the virtual point transformation, flexible interface modes and a transmission simulator, 2018, pp. 205–213. doi:10.1007/978-3-319-74654-8\_18.
- [47] M. van der Seijs (2016).
- [48] M. Haeussler, S. Sendlbeck, D. Rixen, Automated correction of sensor orientation in experimental dynamic substructuring, 2018, pp. 65–70. doi:10.1007/978-3-319-74654-8\_5.
- [49] T. Bregar, A. El Mahmoudi, M. Kodrič, D. Ocepek, F. Trainotti, M. Pogačar, M. Gödeli, G. Čepón, M. Boltežar, D. J. Rixen, pyFBS: A Python package for frequency based substructuring, *The Journal of Open Source Software* 7 (69) (2022) 3399.